

8

Conceptual model for small-volume alkali basalt petrogenesis: implications for volcanic hazards at the proposed Yucca Mountain nuclear waste repository

F. J. Spera and S. J. Fowler

Today, 31 countries operate ~ 450 nuclear power reactors supplying electric power to ~ 1 billion people, $\sim 15\%$ of the world population. Nuclear reactors generate $\sim 17\%$ of global electric power needs and a number of industrialized countries depend on nuclear power for at least half of their electricity. In addition, ~ 30 nuclear power reactors are presently under construction worldwide (Macfarlane and Miller, 2007). A comprehensive summary of the principles, practices, and prospects for nuclear energy may be found in Bodansky (1996). Concerns regarding energy resource availability, climate change, air quality and energy security imply a continuing demand for nuclear power in the world energy budget (Craig *et al.*, 2001). However, to date no country has solved the problem of long-term disposal or storage of nuclear waste. Without a long-term solution, the viability of nuclear energy as an increasingly significant contributor to power generation in the long-range future remains unclear. There is broad consensus that geologic disposal is the safest feasible long-term solution to high-level waste and spent-fuel disposal. Although a number of countries have ongoing geologic repository research programs, there is presently no operational geologic repository for spent fuel or high-level waste on Earth. In the United States, where spent nuclear fuel and high-level waste amounts to $\sim 50\,000$ metric tons, $\sim 15\%$ of the world total, implementation has proven to be challenging both technically and politically. Nuclear waste is currently stored on-site at existing nuclear power stations and at several temporary storage facilities. Permanent geologic disposal, like the siting of a nuclear power plant, requires careful site selection. For geologic disposal, lithology that can isolate radioactive waste from the surrounding environment and biosphere at geologic timescales $\sim 10^4 - 10^6$ a are a minimum requirement (Macfarlane and Ewing, 2006). Of particular importance in this regard are the nature, consequences and probabilities of volcanic hazards that can potentially compromise public, environmental and biospheric safety at long-term nuclear waste storage sites.

Yucca Mountain (YM) in Nevada, USA was identified in the early 1980s as a potential geologic repository for nuclear waste. Yucca Mountain is made up of silicic volcanic tuff-rocks composed chiefly of pyroclastic flow and fall deposits. The proposed Yucca Mountain Repository (YMR) lies on the western boundary of the Nevada Test Site (NTS) within the Basin and Range geologic province (Zoback *et al.*, 1981; Thompson and Burke, 1974). This region is geologically active, with transtensional deformation manifested by faulting, related

seismicity, high $^3\text{He}/^4\text{He}$ anomalies indicative of mantle degassing (Kennedy and van Soest, 2007) and volcanic activity. Intense study of the seismicity, seismic hazards, geohydrology, petrophysics, structural, tectonic and volcanic history of the YM region for over thirty years has provided the geologic foundation for the Total System Performance Assessment (TSPA) used by YM project geoscientists to make probabilistic forecasts of repository behavior. The TSPA considers all potential paths of radionuclides into the environment and defines the US Department of Energy's (DOE) understanding of expected repository performance if built and operated according to present plans. The TSPA forms an integral part of the license application that the DOE submitted to the Nuclear Regulatory Commission (NRC) in June 2008.

The consequences of magmatic disruption of the repository could be very significant in terms of the TSPA regarding radionuclide dispersion. An eruption beneath, into, or through the repository could lead to wide dispersal of radionuclides via atmospheric, surficial (i.e. particulate sedimentation), fluvial and groundwater paths into the biosphere. Therefore it is important to evaluate the probability and consequences of potentially disruptive magmatic events. The consequences of disruption evidently depend on the characteristics of a magmatic event (e.g. eruptive style and volume, magma properties and dynamics, volatile content of magmas, etc). A disruptive igneous event within the footprint of the repository has been estimated to have a rather low occurrence probability of 1 event in 70 Ma, with a 90% confidence interval ranging from 1 event in 20 Ma to 1 event in 180 Ma (Geomatrix Consultants, 1996). Independent of the DOE, the NRC has estimated volcanically-induced disruptive event probabilities in the range of 1 event in 10 Ma to 1 event in 100 Ma.

In this study we present a sketch of a conceptual model consistent with the eruption dynamics, petrology, major and trace element geochemistry of small-volume alkali basaltic volcanism in the YM region. In particular, the generation, modification upon ascent, and eruption of alkali basaltic magma to form small-volume volcanic constructs of lava and tephra is considered in some detail. This style of eruption, in our opinion, is the type most relevant to possible future eruptions at or near YM. Quantitative evaluation of volcanic hazards including eruption forecasting ultimately requires integration of comprehensive quantitative models of petrogenesis (*sensu lato*) into the regional geological framework. The aim of this study is to present a birds-eye-view of small-eruptive volume alkali basalt petrogenesis relevant to evaluation of magmatic hazards at the proposed permanent nuclear waste repository at Yucca Mountain, Nevada, USA.

8.1 Volcanic hazard evaluation

Evaluation of volcanic hazards at YM is aided by understanding the fundamental nature of regional volcanism. Results of previous geologic investigations of YM and environs clearly indicate a proclivity for small-volume basalt eruptions, as opposed to, for example, large-volume, highly explosive silicic eruptions. However, evaluation of volcanic hazards at YM is complicated compared to traditional volcanic hazard studies that assess the possibility of future eruption at an existing volcano, because volcanism forecasting relevant to the

YMR involves an event at a specific location where volcanism has not occurred in the last 10 Ma. Volcanic hazard evaluation and prediction at YM therefore involves the coupled and difficult problems of predicting the timing, location, volume and eruptive style of possible eruptive events. Any single one of these issues can be complicated; together they represent a very challenging problem. In addition, high-resolution modeling of magmatic phenomena and eruption forecasting is itself complicated by the complex nature of dynamic processes in magmatic systems, which are non-linear at multiple spatial and temporal scales (Shaw, 1987), and the inherently stochastic distribution of heterogeneity at all scales in geologic media such as the upper crust beneath YM.

Information necessary for assessing the probability and consequences of a future disruptive magmatic event (volcanic eruption or intrusion by dike or sill at the repository depth) at YM includes the eruptive style(s) (e.g. pyroclastic flows or falls, lava flows, lahars, phreatomagmatic explosions, etc), spatial and temporal distribution and number of previous events, as well as the distribution and geometric properties of the subsurface magma transport system (dikes, sills, hypabyssal intrusions, conduits). Assessing associated uncertainties is as important as defining mean values or average types of behavior. Constraints derive from, for example, careful study of analog volcanic provinces, including older, exhumed terrains, in the context of the regional geologic and geophysical setting, as well as application of dynamical, phase equilibria, and trace element models relevant to magma generation, transport, reaction, and eruption based on thermodynamics, fracture mechanics, fluid dynamics and geochemistry.

This paper is organized as follows. In the next section, a brief summary of YM region volcanism is given. This provides a basis for inferring the most likely composition, volume, volatile content and eruptive style of volcanic events in the next ten thousand to one million years. Based on this determination, we consider stages in magma transport from source to surface. These stages include the phase equilibria and thermodynamics of partial melting; segregation; mobilization and ascent of magma through the lithosphere; and finally, near-surface flow of magma, driven mainly by volatile exsolution.

8.1.1 Volcanological and tectonic background

Over the past thirty years, many studies have addressed the age, geochemistry, petrology, volcanology and magma properties relevant to magmatic activity in the greater Yucca Mountain region. It is beyond the scope of this work to review this literature. A few recent studies that serve as links to earlier work include Smith *et al.* (1990), Fleck *et al.* (1996), Perry *et al.* (1998), Valentine *et al.* (1998), Perry and Youngs (2000) and Smith *et al.* (2002). The report of Detournay *et al.* (2003) summarizes the history of volcanism, describes magma thermodynamic and transport properties and addresses the likely characteristics of a future volcanic event at YM based on past volcanic activity, with a focus upon the past 5 Ma. The consequences of repository disruption by an igneous event are discussed in Detournay *et al.* (2003), Woods *et al.* (2002), Menand *et al.* (Chapter 17, this volume) and Valentine and Perry (Chapter 19, this volume). Crowe *et al.* (2006) present an overview of the volcanism

problem, how it has been studied historically in the context of the YM project and its potential impact on an underground repository. The study of Fridrich *et al.* (1999) provides a thorough account of the tectonics, especially the evidence and timing (mainly Miocene) of extension in the YM region. Regional volcanism is summarized in Perry *et al.* (1998). Lathrop Wells, the youngest volcano in the region is described in detail by Perry and Straub (1996), Valentine and Perry (2007) and Valentine *et al.* (2006). We draw upon these studies in the summary below.

A regional map that highlights recent volcanism around YM is given in Figure 8.1. Yucca Mountain (*sensu stricto*) is composed of Miocene silicic volcanic rocks representing deposits from a series of large-volume eruptions associated with several large calderas north of the mountain. The most proximate one is the Timber Mountain caldera north of YM. Silicic pyroclastic eruptive activity began ~ 15 Ma and ceased ~ 8 Ma. Patterns of silicic ignimbrite-forming events in the Great Basin over the past 30 Ma indicate that further large-volume silicic pyroclastic flow and fall eruptions are not likely to recur in the YM region within the next few million years. Late Miocene–Quaternary basaltic volcanic activity succeeded Miocene silicic volcanism in the YM region. The basalts can be divided into two major episodes. Basalt of the silicic episode erupted during the waning stage of silicic volcanism (> 8 Ma), whereas eruptions of post-caldera basalt began more recently and continue into the Quaternary. The post-caldera episode can be further subdivided into older post-caldera basalts outcropping north, northeast, and southeast of YM (Figure 8.1), and younger post-caldera basalts, which crop out west, southwest, and south of YM. The older post-caldera basalts range in age from ~ 9 – 6 Ma. An apparent volcanic hiatus of about two and a half million years (from ~ 7.2 – 4.7 Ma) separates the older and younger post-caldera basalts.

In order of decreasing age, the younger (Pliocene–Quaternary) basaltic volcanics (lava flows and tephra deposits) include the Pliocene basalts of Thirsty Mesa (4.7 Ma; volume, $V \sim 2.6$ km³) and southeast Crater Flat (3.7 Ma; $V \sim 0.6$ km³), the 3.1 Ma basaltic trachyandesites of Buckboard Mesa ($V \sim 0.8$ km³), the five Quaternary (~ 1 Ma) alkali basalt cones of Crater Flat of total volume ~ 0.15 km³, the 0.35 Ma basalt cones of Hidden Cone and Little Black Peak at Sleeping Butte ($V \sim 0.05$ km³), and the most recent eruption in the area, the 78 ka, ~ 0.1 km³ Lathrop Wells alkali basalt cone and lava field located ~ 20 km south of the YMR footprint. Within the last million years, eruptions near YM have all been small volume; deposits include both tephra fallout and lava flows of alkali basalt (nepheline normative) composition.

In addition to exposed volcanic deposits, a number of buried basaltic lava flows or small intrusive bodies inferred from geomagnetic surveys lie beneath alluvial fan deposits in the shallow subsurface southwest (Crater Flat) and southeast (Jackass Flats) of YM (Figure 8.1). Drilling and geochronological, geochemical and petrographic examination of these bodies has been conducted at the following locations (refer to Figure 8.1): (i) the 11.3 Ma basalt of magnetic anomalies **Q** (**R** and **4**, probably related to **Q**) and **T** located northwest of the ~ 1.1 Ma Red and Black cones in Crater Flat, east of the Bare Mountain fault at the western edge of the Amargosa trough, (ii) anomaly **A**, a 10.1 Ma basanite located due south

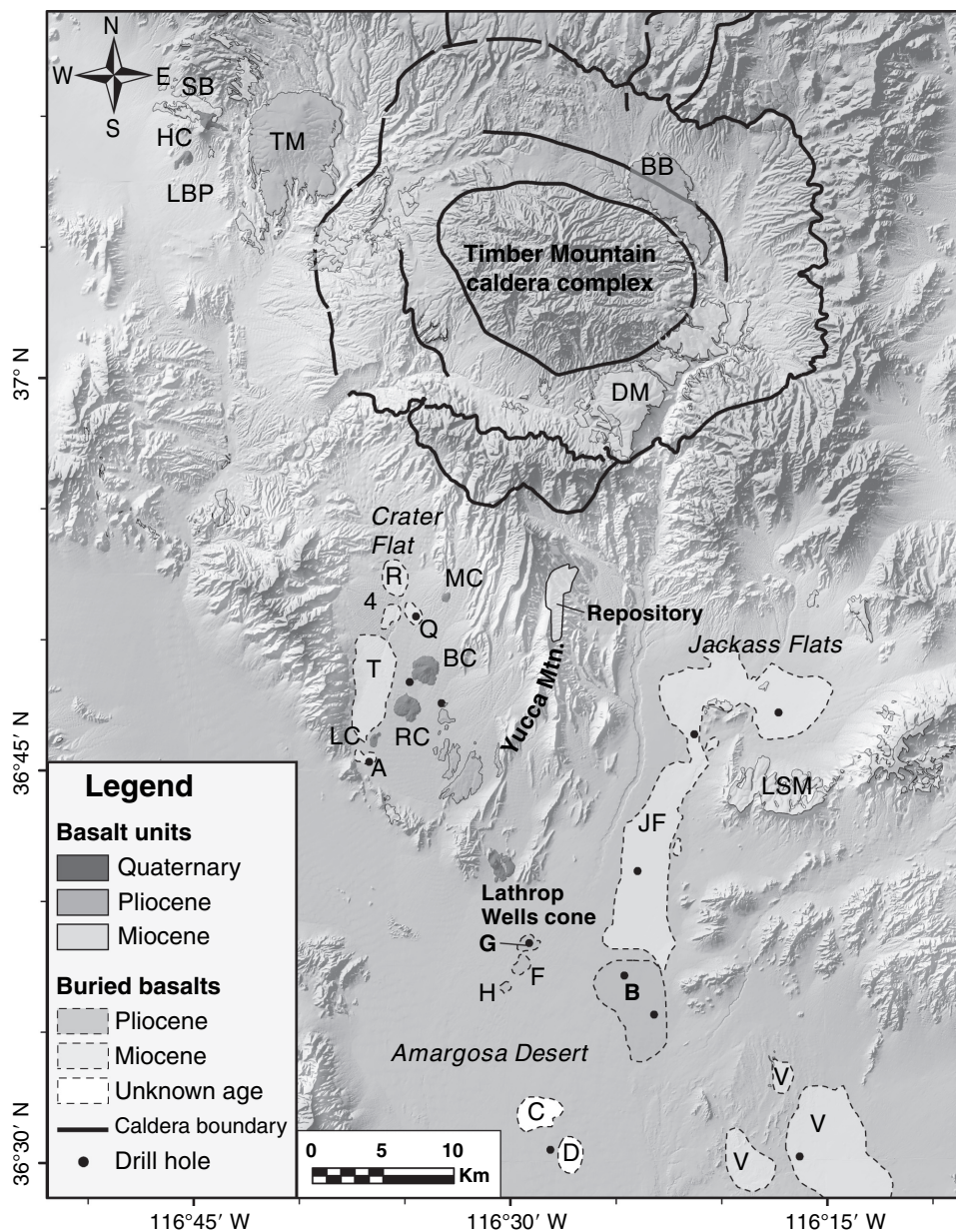


Fig. 8.1 Basaltic volcanoes in the YM region. Buried Pliocene and Miocene basalts (dashed outline) identified by magnetic anomalies, drilling and sample geochronology. Miocene caldera boundary is black line. Miocene volcanic rocks: Sleeping Buttes (SB), Dome Mountain (DM), Little Skull Mountain (LSM). Pliocene volcanic rocks: Thirsty Mesa (TM), Buckboard Mesa (BB). Quaternary volcanoes: (1.1 Ma): Makani (MC), Black Cone (BC), Red Cone (RC), Northeast and Southwest Little Cones (LC); (0.35 Ma): Little Black Peak (LBP), Hidden Cone (HC). 77 ka Lathrop Wells volcano. Magnetic anomalies: A–D, F–H, Q, R, T, V, 4. Map provided by Dr. Frank V. Perry of Los Alamos National Laboratory. See color plate section.

of anomaly **T** and the Quaternary Little Cones, (iii) a large-area magnetic anomaly in Jackass Flats of age ~ 9.5 Ma mainly south and east of YM forming the eastern boundary of the Amargosa trough, and (iv) the buried basalts of anomalies **V** (9.5 Ma), **B** (3.8 Ma), and **G** (**F** and **H** probably related to **G**) dated at 3.8 Ma. Several additional magnetic anomalies, inferred to be buried volcanics based on their locations and magnetic signatures, have not been sampled (e.g. anomalies **C** and **D**). Although anomalies **C** and **D** have not been dated radiometrically, estimates based on depth of burial and alluvial fan sedimentation rates suggest an age 4.2–5.8 Ma.

Except for the basaltic andesite of Buckboard Mesa and the basalt of anomaly **B**, all younger post-caldera exposed basalts lie within a 10 km wide northwest-trending zone west of YM in the Crater Flat–Amargosa trough corridor. This zone extends from the small-volume basalts of Sleeping Butte south through the Quaternary and Pliocene basalts of Crater Flat and continues south to Lathrop Wells and buried Pliocene basaltic deposits in the Amargosa Valley.

8.1.2 Expected event: composition, volume and style

Discrete events in the region in the last few million years are characterized by small-volume ($0.01 \text{ km}^3 - 1 \text{ km}^3$) alkali basaltic lava and tephra eruptions. Based on modern analogs, typical eruption durations are measured in terms of days, weeks, or months and depend primarily on the total volume of magma erupted. Eruptive fluxes in the range $10^3 - 10^4 \text{ kg m}^{-2} \text{ s}^{-1}$ lead to mass flows of order $10^5 - 10^7 \text{ kg s}^{-1}$ based on typical conduit cross-sectional areas observed in ancient analog systems (e.g. Detournay *et al.*, 2003). Eruptions at the high end of these ranges could produce Strombolian eruption plumes up to 10 km high; more typical eruptions would produce plume heights of order several kilometers. The volatile content, inferred from phase equilibria, the study of glass inclusions in phenocrysts, and the order of low-pressure, near-surface crystallization of microphenocrysts, lies in the range 2.5–4 wt.%, with H_2O the dominant fluid species (Detournay *et al.*, 2003). The dissolved volatile content of rising magma plays a critical role in determining eruptive style. A dynamical transition occurs when the volume fraction of the fluid phase in magma exceeds the critical volume fraction (θ_{crit}) for magma fragmentation $\sim 0.5 - 0.7$. There is a rapid decrease in magma density and increase in magma (mixture) compressibility around this rheological transition. These magma property variations lead to rapid increases in magma eruptive velocity near the fragmentation depth. The depth at which magma fragmentation occurs depends upon the dissolved volatile content of magma and the dependence of volatile solubility on temperature, pressure and melt composition. It also depends on whether or not volatiles can leak from the magma into surrounding crustal rocks. These issues are quantified in Section 8.5.3. Although not discussed here, phreatomagmatic-style eruptions, in which magma encounters low-temperature, water-saturated permeable crust to generate steam-rich violent eruptions, are possible in wetter climates than now observed at YM. Musgrove and Schrag (2006) have analyzed possible future climates, specifically wetter conditions associated with a higher water table, in the southern Great Basin. They noted that the most

recent time in Earth history when CO₂ levels approached those anticipated in the next few hundred years was in the Eocene. Consideration of Eocene-like climate scenarios may therefore provide some lessons about possible climate changes due to increased (anthropogenic) CO₂. The design of the repository should account for the potential risk of significantly wetter conditions at YM that would enhance the chances for phreatomagmatic-style eruptions. In the remainder of this chapter, phreatomagmatic eruptions are not explicitly considered.

8.2 Magma generation and transport: a source to surface overview

Several topics related to the generation, segregation, ascent, and eruption of basaltic magma, and the results in light of volcanic hazards at YM, are considered. We adopt as typical of future eruptive activity in the Yucca Mountain region the 78 ka, ~ 0.1 km³ alkali basaltic lava and tephra eruption at Lathrop Wells, ~ 20 km south of the proposed YMR. Although the generation and transport of magma is a continuum process, it is convenient to analyze successive stages from melt generation to eruption or shallow-level intrusion. The self-consistent, thermodynamically based pMELTS and MELTS phase-equilibria models of Ghiorso *et al.* (2002) are used to perform calculations that account for important sources of variability in liquid compositions and their physical properties. Extensive documentation of the phase-equilibria algorithms is presented elsewhere (e.g. Hirschmann *et al.*, 1998; Hirschmann *et al.*, 1999a; 1999b; Ghiorso *et al.*, 2002; Asimow and Longhi, 2004). Although no phase-equilibria model is perfect due to the thermodynamic complexities of multicomponent–multiphase silicate systems, the MELTS algorithm has been repeatedly shown to faithfully capture multicomponent phase relations in mafic–ultramafic systems. Petrogenesis from phase equilibria includes forward modeling of primary melt generation via partial melting of a peridotitic source and primary melt modification by fractional crystallization during upward ascent of primary melt. In particular, we compare melt compositions resulting from forward modeling of partial melting and fractional crystallization to the available volcanologic, geochemical and petrologic database for Lathrop Wells (Perry and Straub, 1996; Valentine *et al.*, 2006; Valentine and Perry, 2007). The phase-equilibria results link heat transfer between magma and surrounding lithosphere to the fracture mechanisms that drive magma ascent beneath Yucca Mountain, where the large-scale extensional stress environment of the Great Basin aids buoyancy-driven upward propagation of magma-filled crack networks. As magma ascends to the near surface, new dynamic processes become important. Once a magmatic mixture develops an appreciable volume fraction of fluid (bubbles), the behavior of the compressible dynamics of magma (melt plus fluid) becomes important. The dispersal of ash and lava from a small-volume alkali basalt volcano is very relevant to magmatic hazard analysis at YM.

The initial step leading to small-volume alkali basaltic eruption is partial melting of peridotite in the upper mantle. Factors that govern the composition of primary melt include the extent to which partial melt stays in chemical potential equilibrium with the crystalline residue, the composition of source peridotite (i.e. mineral compositions and abundances, water content and redox state) and the mean pressure of partial melting. The effects of

each of these parameters are tested by performing approximately 80 partial melting simulations, systematically varying the governing parameters. Below, results for representative cases to illustrate parameter sensitivity are presented. The melting scenario that produces primary partial melt is analyzed in detail. This melt, upon further evolution by fractional crystallization, exhibits a composition corresponding most closely to Lathrop Wells basalt. Liquid ferric iron to ferrous iron ratios are based on the oxygen fugacity constraint along the QFM-1 buffer (i.e. one log base-ten unit below the Quartz–Fayalite–Magnetite buffer). A number of sensitivity tests are performed to explore the effects of varying oxygen fugacity. These effects are found to be minor compared to variations of other intensive parameters such as pressure or source fertility.

8.2.1 Source bulk compositions

Table 8.1 gives the anhydrous major element compositions of three end-member ultramafic compositions used in the phase-equilibria simulations. Composition **1B-33** (Bergmann, 1982) corresponds to a depleted harzburgite xenolith from a 38 ± 10 ka lava flow within the Lunar Crater volcanic field, Nevada (Yogodzinski, 1996), located several hundred kilometers northeast of YM. Composition **1B-33** represents the most depleted of the compositions used in this study. Composition **PA-12** (Frey and Prinz, 1978) is a moderately fertile peridotite xenolith from the Pleistocene basaltic vent at Peridot Mesa in the San Carlos volcanic field, Arizona, USA. The most fertile peridotite composition used in this study, **KLB-1** (Hirose and Kushiro, 1993), is a garnet peridotite xenolith from Kilbourne Hole, New Mexico, USA (Padovani and Reid, 1989). The Kilbourne Hole maar, a phreatomagmatic explosion crater, formed when the Afton basalt intermingled with wet rift-fill sediments in the Camp Rice Formation of the Santa Fe Group. The age of the phreatomagmatic explosion and basalt eruption responsible for creating the Kilbourne Hole maar is 77 ka (Anthony and Poths 1992). The compositions are peridotitic, but differ in terms of fertility. Fertility refers to the potential of a peridotite to generate basaltic liquid (melt) by partial melting. There is no strict definition of fertility; several measures of fertility are given in Table 8.2. In particular, the mass ratio of the phases amphibole + phlogopite + clinopyroxene + garnet relative to olivine + orthopyroxene at the solidus pressure; modal clinopyroxene; the mass ratio of FeO/MgO in the peridotite source; and relatively high values for Al_2O_3 , TiO_2 and CaO all positively correlate with peridotite fertility. Fertility increases from **1B-33** (depleted) to **PA-12** (moderately fertile) to **KLB-1** (fertile). To each anhydrous bulk composition in Table 8.1, 0.2 wt. % H_2O has been added. At 1.5 GPa amphibole (Amp) and phlogopite (Phl) are present in the fertile compositions at the solidus. Garnet (Gt) and phlogopitic mica are present at 3.5 GPa.

8.2.2 Fractional or batch melting?

There are two end-member models relevant to partial melting. In batch partial melting, melt remains in chemical potential equilibrium with crystalline residue during progressive

Table 8.1. Anhydrous composition of peridotites

Wt. %	1B-33	PA-12	KLB-1
SiO ₂	43.96	43.66	44.59
TiO ₂	0.03	0.02	0.16
Al ₂ O ₃	1.85	3.13	3.60
Cr ₂ O ₃	na	0.30	0.31
FeO	7.48	7.98	8.12
MnO	0.15	0.15	0.12
MgO	45.42	42.89	39.32
CaO	1.02	1.41	3.45
Na ₂ O	0.05	0.31	0.30
K ₂ O	0.03	0.12	0.03
P ₂ O ₅	na	0.02	na

Table 8.2. Mineralogy and fertility measures for peridotite starting compositions

Sample	Mass fraction ¹		Wt. % alkalies	Wt. % FeO/MgO	Wt. % MgO
	Amp + Phl + Cpx + Gt/Ol + Sp + Opx				
	1.5 GPa	3.5 GPa			
1B-33	0.036	0.067	0.08	0.16	45.4
Lunar Crater	Ol ² ,Opx,Gt,Cpx	Ol,Opx,Gt,Cpx,Phl			
PA-12	0.083	0.152	0.43	0.19	42.9
San Carlos	Ol,Opx,Cpx,Amp,Sp,Phl	Ol,Opx,Gt,Cpx,Phl,Sp			
KLB-1	0.190	0.325	0.33	0.21	39.3
Kilbourne Hole	Ol,Opx,Cpx,Amp,Sp,Phl	Ol,Opx,Cpx,Gt,Sp,Phl			

¹ Phase abundances are at solidus temperature at indicated pressure with 0.2 wt. % H₂O added to the anhydrous compositions of Table 8.1. The redox condition is QFM-1 in all cases.

² Order of phase listing is from most to least modal abundance at the prescribed pressure.

fusion until melt is segregated from source crystals at some fixed value of the extent of melting, either 5%, 10% or 15% melting (by mass) in this study. In fractional partial melting, melt is isolated from crystalline residue immediately and completely upon generation; no further reaction occurs between melt and residual crystals. In reality, the mode of partial melting in the Earth lies between these limits. We compared results of fractional and batch partial melting for all three starting compositions. Figure 8.2 shows MgO variation diagrams for the compositional sequence of partial melts generated by fractional and batch partial melting for starting composition **KLB-1** (fertile peridotite; Table 8.1) plus 0.2 wt. % H₂O.

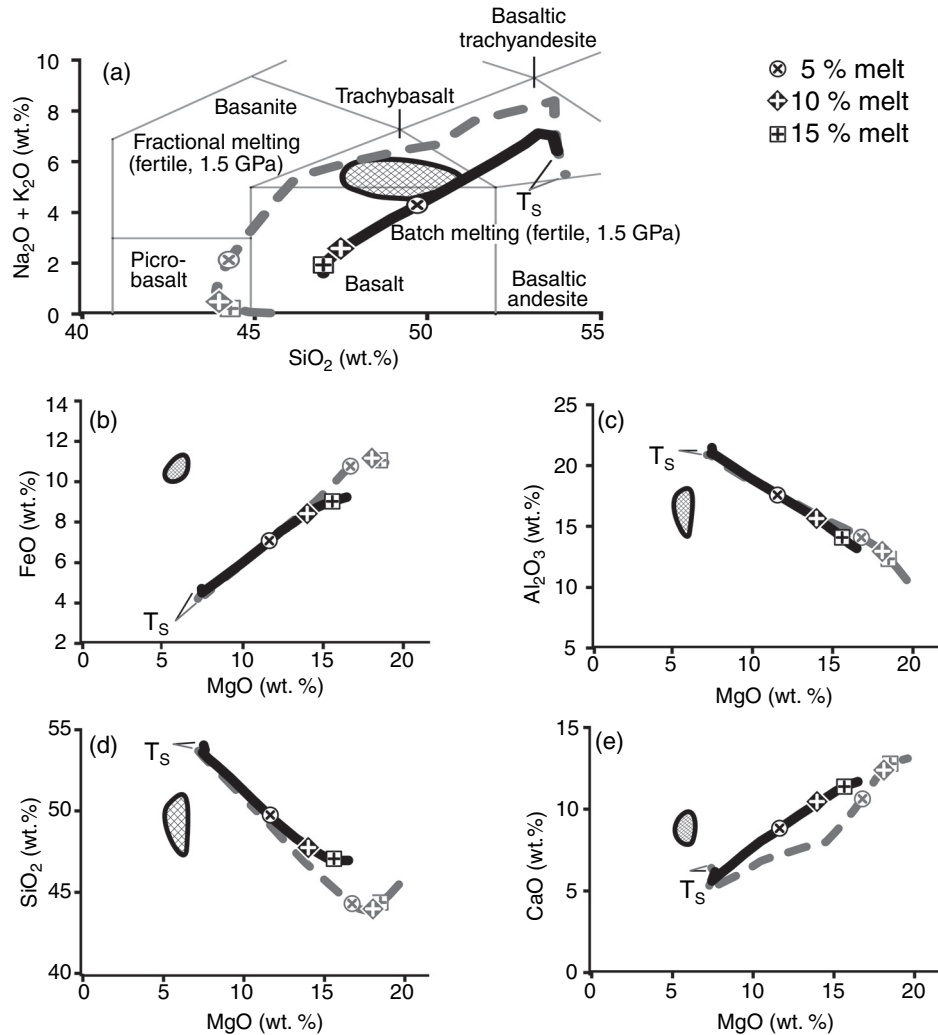


Fig. 8.2 comparison of isobaric fractional (grey dashed line) and batch (solid black line) partial melting phase-equilibria calculations using the pMELTS algorithm for fertile peridotite bulk composition **KLB-1** (Hirose and Kushiro, 1993). Oxygen fugacity is fixed along the QFM-1 buffer. Increasing wt. % MgO and decreasing wt. % ($\text{Na}_2\text{O} + \text{K}_2\text{O}$) correspond to increasing magma temperature. The beginning of each pMELTS trend is labeled T_s . Cross marks within circle, diamond and square outlines, signify 5%, 10%, and 15% melting, respectively. The termination of each pMELTS trend corresponds to a melt fraction of 20%. The shaded region represents the field of Lathrop Wells data (Perry and Straub, 1996; Valentine and Perry, 2007). The data field is not expected to coincide with the pMELTS trends due to the non-primary nature of Lathrop Wells basalt (see text for further details). Plots of major element variations versus MgO (a–e) document the trajectory of melt compositions during batch and fractional melting of fertile peridotite. The total alkalis–silica diagram is based on the classification scheme of Le Maitre *et al.* (1989).

Oxygen fugacity is constrained at QFM-1 and the pressure of isobaric melting is 1.5 GPa, corresponding to a depth ~ 50 km beneath Yucca Mountain. The solidus is marked T_s and points are labeled on the liquid curves representing 5%, 10% and 15% partial melting by mass. The melt composition at the thermodynamic solidus where the ‘trace’ of melt is present, is, by definition, identical for batch and fractional melting. In Section 8.3 we present fractional crystallization calculation results indicating that batch partial melting better represents mantle partial melting than fractional partial melting. In short, fractional crystallization models based on melts derived from fractional partial melting produce liquids that deviate widely from observed compositions at Lathrop Wells, whereas batch partial melting generates liquids that, on undergoing fractional crystallization, coincide quite well with observed Lathrop Wells major and trace element data. Based on trace element arguments, it is generally agreed that the degree of melting (by mass) of a peridotite source to produce basalt is in the range 5–10%. All results reported on hereafter refer to batch partial melting with extent of melting between 0–15%.

8.2.3 Role of peridotite fertility

We investigate the importance of peridotite fertility via partial melting computations based on the three peridotites of Table 8.1; 0.2 wt. % H_2O has been added to each anhydrous bulk composition. Table 8.2 gives the solidus phase assemblage for each bulk composition, calculated by Gibbs energy minimization at 1.5 and 3.5 GPa. Small amounts of modal amphibole and phlogopite (hydrous phases) are present at the 1.5 GPa solidus for the more fertile compositions **PA-12** and **KLB-1**. Figure 8.3a–e depicts the composition of melts generated by batch partial melting at 1.5 and 3.5 GPa on MgO variation diagrams. The symbols along each curve indicate 5%, 10% and 15% melting by mass. The composition of melt at the solidus is marked T_s . The Lathrop Wells basalt compositional field, shown as a shaded field, is for reference only. Since Lathrop Wells basalt is not primary melt (its Mg# is far too low), calculated partial melt compositions are not expected to cross the Lathrop Wells field. However, because we expect that primary melt evolves to Lathrop Wells melt by fractional crystallization, the starting composition along the batch partial melting curve must lie at a location in composition space such that fractional crystallization of the primary melt drives the liquid composition into the Lathrop Wells field. We demonstrate in Section 8.3.1 that a fertile (**KLB-1**) or moderately fertile (**PA-12**) source undergoing partial melting at relatively low pressure (1.5–2 GPa) does indeed provide a composition, which upon subsequent fractional crystallization during ascent, evolves into the Lathrop Wells compositional field. This is especially clear on the CaO and total alkalies MgO variation diagrams. The batch partial melting generated by 5%, 10% or even 15% partial melting of a depleted source cannot evolve by fractional crystallization into the Lathrop Wells field. In addition, batch partial melting at 3.5 GPa generates liquids that do not, upon subsequent crystal fractionation, evolve into the Lathrop Wells compositional field. We conclude that the mantle source for Lathrop Wells basalt was fertile or moderately fertile and that the mean pressure of partial melting was significantly closer to 1.5 GPa (~ 50 km) than 3.5 GPa (110 km). The effects of melting pressure are examined in more detail below.

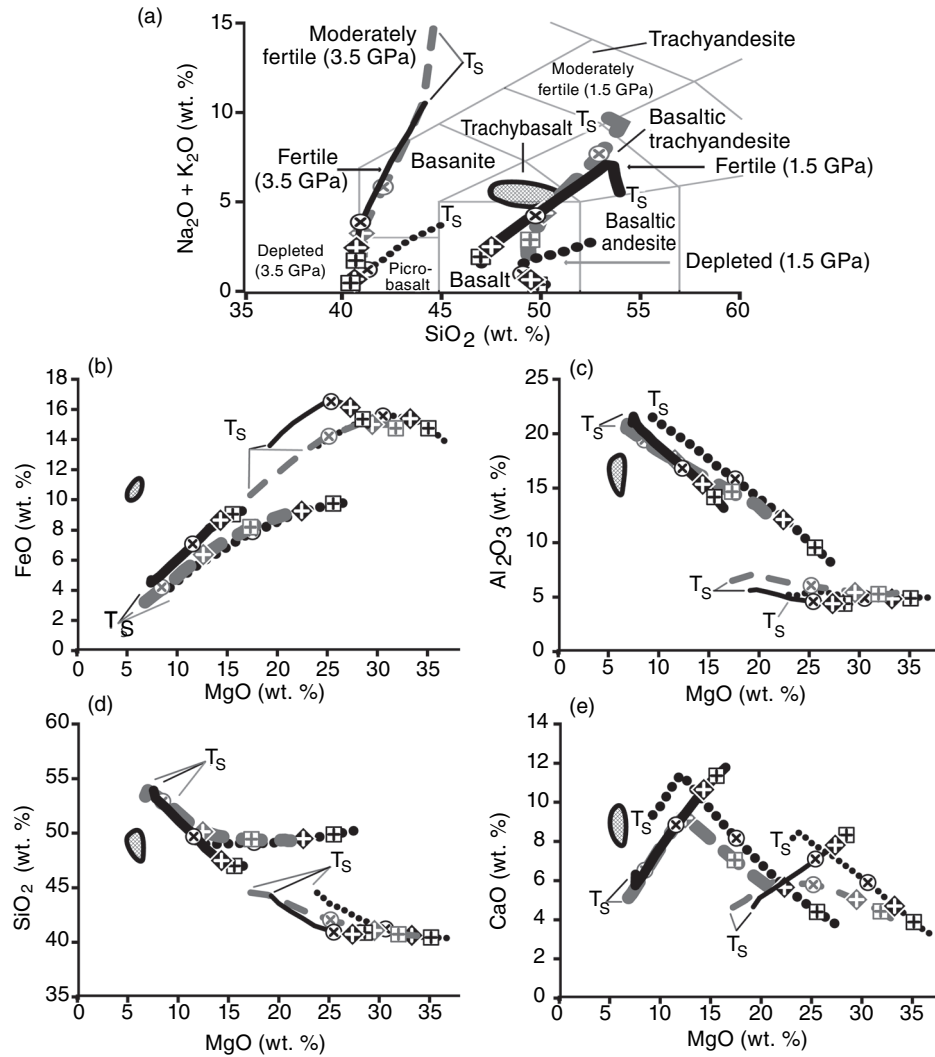


Fig. 8.3 Results of isobaric pMELTS batch partial melting calculations at 1.5 GPa (large symbols) and 3.5 GPa (small symbols) for depleted, moderately fertile and fertile peridotite. Compositions are given in Table 8.2; dotted line: depleted peridotite **1B-33** (Bergman, 1982); dashed grey line: moderately fertile peridotite **PA-12** (Frey and Prinz, 1978); solid black line: fertile peridotite **KLB-1** (Hirose and Kushiro, 1993). All other parameters and abbreviations are identical to Figure 8.2.

8.2.4 Role of pressure on composition of partial melting

The role of pressure in modifying the composition of peridotite batch partial melts has been studied in detail. The starting composition is fertile **KLB-1** plus 0.2 wt. % H_2O . The redox condition is fixed along the QFM-1 buffer. The MgO variation diagrams showing the

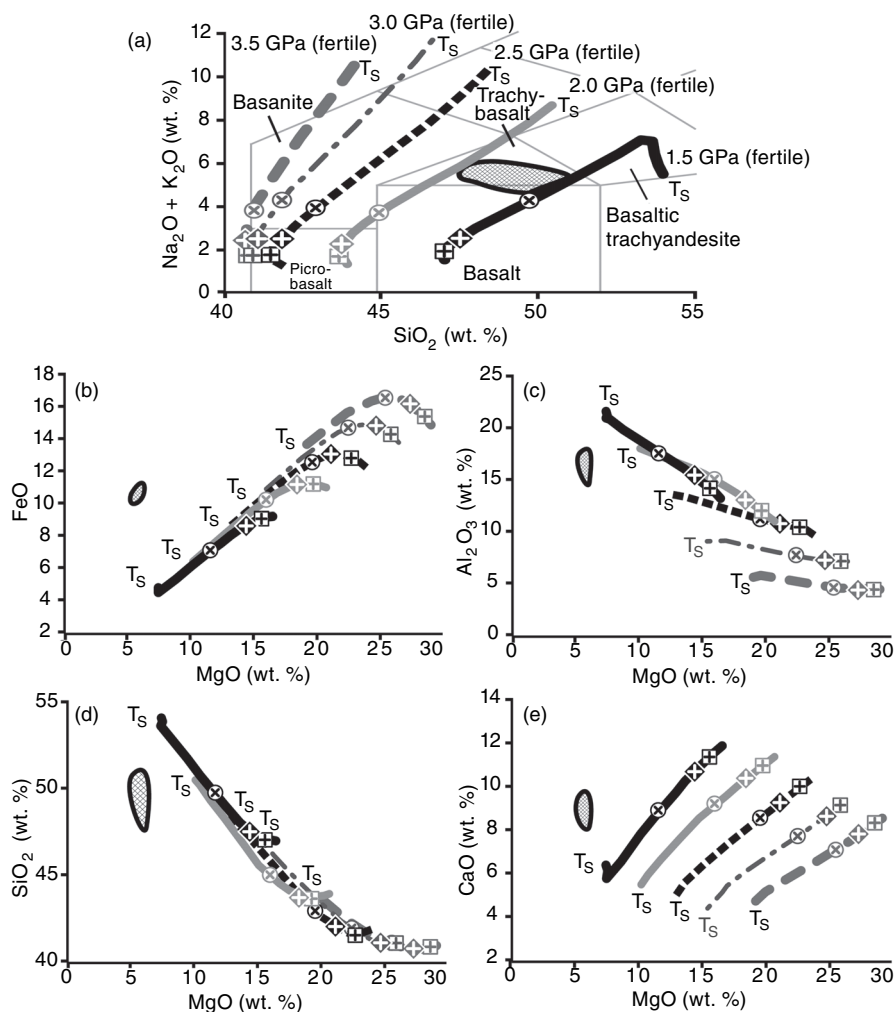


Fig. 8.4 pMELTS isobaric batch partial melting trends based on fertile peridotite **KLB-1** (Hirose and Kushiro, 1993) for varying pressures; solid black line: 1.5 GPa; solid grey line: 2.0 GPa; dotted black line: 2.5 GPa; dot-dashed line: 3.0 GPa, dashed grey line: 3.5 GPa. All other parameters and abbreviations are identical to Figure 8.2. Isobaric partial melting at pressures greater than 2 GPa generate melts that do not evolve into the Lathrup Wells field upon fractional crystallization. Melts generated by partial melting for pressures in the range of 1.5–2.0 GPa evolve into the Lathrup Wells field upon subsequent fractional crystallization.

compositional sequence of batch partial melts starting at the solidus are shown in Figure 8.4 for pressures of 1.5, 2.0, 2.5, 3.0 and 3.5 GPa. These pressures span a depth range \sim 50–110 km beneath Yucca Mountain. The effect of increasing pressure at fixed melt fraction (e.g. 5 wt. %) is to increase MgO and FeO and reduce the Al_2O_3 content of partial melt.

An important result of these calculations is that high-pressure partial melting can be ruled out. For example, the FeO vs. MgO plot (Figure 8.4b) shows that partial melts generated at pressures ≤ 2 GPa are less FeO rich than high-pressure melts at the same extent of melting. Because fractional crystallization of basaltic melt drives derivative liquids to higher FeO, it is clear that fractional crystallization of a high-pressure partial melt cannot drive a primary melt into the Lathrop Wells field. The conclusion is that the pressure of partial melting for generation of the primary Lathrop Wells basalt liquid is in the range 1.5–2 GPa ($\sim 52 - 67$ km beneath Yucca Mountain).

8.2.5 Role of H₂O content in source peridotite

A series of hydrous melting calculations based on a variety of source H₂O contents were performed to explore the effect of H₂O on melting of fertile peridotite **KLB-1**. Figure 8.5 shows the calculated compositional paths for batch melting at 1.5 GPa, with oxygen fugacity at QFM-1. The plotted results correspond to four distinct source water contents: dry, 0.1 wt. % H₂O, 0.2 wt. % H₂O and 0.6 wt. % H₂O. The symbol boxes along the melt lines refer to 5%, 10% and 15% melting. The solidus is marked by T_s. An initial H₂O concentration of 0.6 wt. % exceeds the storage capacity of melt and hydrous minerals (amphibole and phlogopite) and leads to a hydrous fluid phase at the solidus, a somewhat unlikely condition in general given inferences of the average water content of typical mantle peridotites (Carlson and Miller, 2003; Asimow and Langmuir, 2003). For a fixed fraction of partial melt (e.g. 5%) the alkali–silica diagram (Figure 8.5a) shows that partial melts become increasingly silica-rich (from ~ 46 –53 wt. % SiO₂) with increasing initial H₂O content, although the total alkali content of the melt remains constant around 4 wt. %. The criterion that pMELTS liquid H₂O concentration predictions at the end of fractional crystallization must coincide with inferred pre-eruptive Lathrop Wells H₂O concentrations of 2.5–4 wt. % (Detournay *et al.*, 2003) leads to the conclusion that source water contents lie in the range 0.1–0.3 wt. %. We have chosen to present pMELTS results based on a representative starting H₂O concentration of 0.2 wt. %. Dry partial melts are too alumina and silica poor and too FeO rich to evolve by fractional crystallization into the Lathrop Wells field.

8.2.6 Summary of partial melting conditions

More than 100 phase-equilibria simulations were conducted using the pMELTS algorithm of (Ghiorso *et al.*, 2002) in which systematic variation of several critical factors (melting process, source fertility, pressure of melting and source H₂O content) were studied. Evaluation of the quality of results is based on the criterion that fractional crystallization of primary partial melts of a fertile peridotitic source should give rise to a predicted melt composition similar to that observed for Lathrop Wells basalt. The most plausible melting scenario is a 5–10% batch melting of a fertile peridotite (olivine, orthopyroxene, clinopyroxene, spinel, amphibole and phlogopite) with an initial water content of ≈ 0.2 wt. % H₂O along the QFM-1 buffer curve at 1.5–2 GPa (~ 50 –70 km depth). At either 5% or 10% melting,

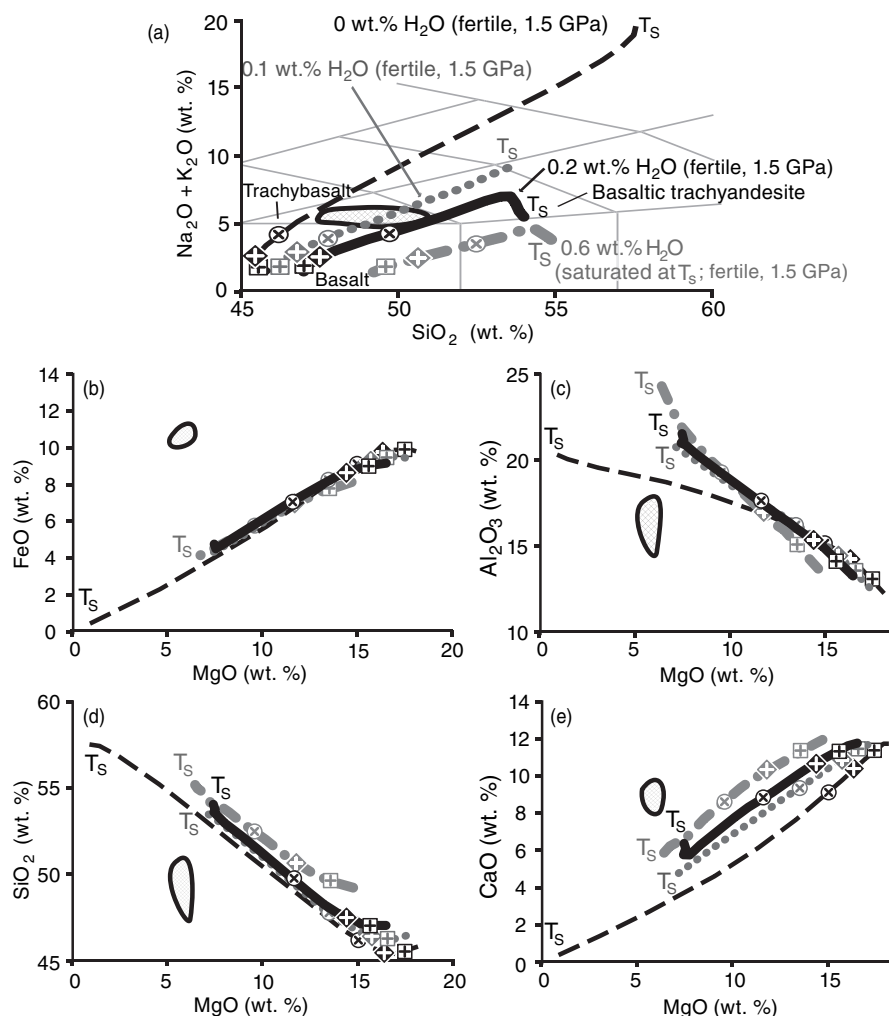


Fig. 8.5 Results of numerical experiments designed to examine batch partial melting of pMELTS liquid compositions with varying initial bulk water contents. The source composition is fertile peridotite **KLB-1** (Hirose and Kushiro, 1993); dashed black line: anhydrous; dotted grey line: 0.1 wt. % H_2O ; solid black line: 0.2 wt. % H_2O ; dashed grey line: 0.6 wt. % H_2O . All other parameters and abbreviations are identical to Figure 8.2. Hereafter, the 0.2 wt. % H_2O case is used as the reference case.

the residual source assemblage is olivine, orthopyroxene, clinopyroxene and spinel. The temperatures and dissolved H_2O contents of primary melt generated at 5% and 10% melting are 1280 °C and 1350 °C, and 3.3 wt. % H_2O and 1.74 wt. % H_2O , respectively at 1.5 GPa. The Mg # (\equiv atomic $\text{Mg}/(\text{Mg} + \text{Fe}^{+2})$) of the 5% and 10% partial melts are 76 and 77, respectively. The mineral proportion diagram for batch partial melting of fertile peridotite

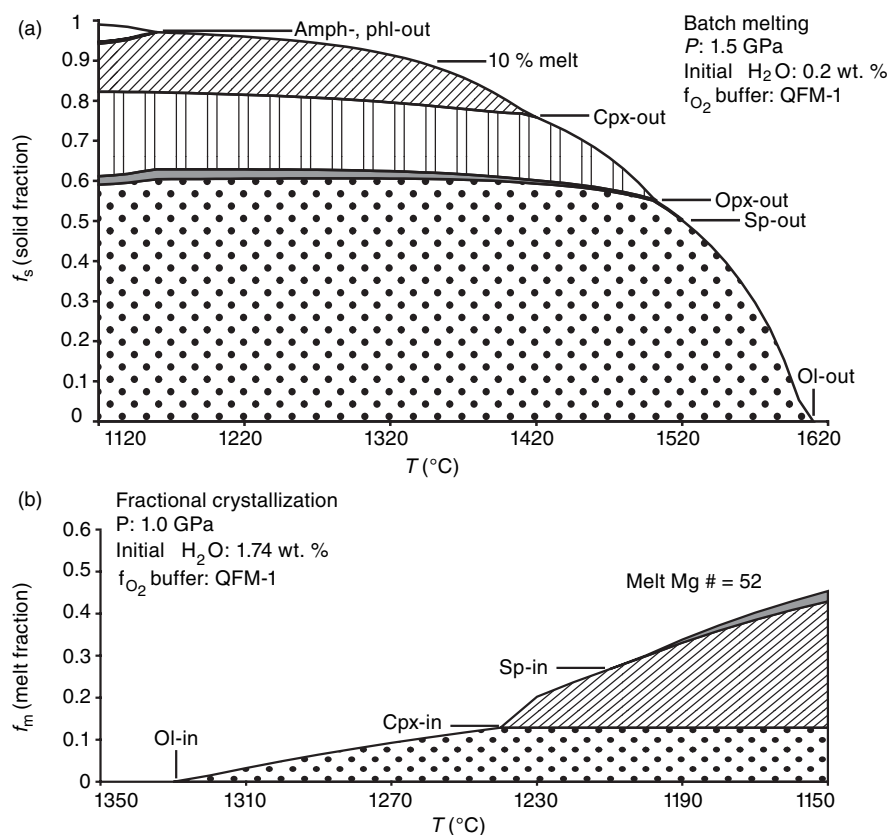


Fig. 8.6 Phase proportions as a function of temperature (T) based on (a) batch partial melting of fertile peridotite **KLB-1** (Hirose and Kushiro, 1993) plus 0.2 wt. % H_2O at 1.5 GPa; the 10% partial melt has a dissolved H_2O content of 1.74% at ~ 1310 °C at 1.5 GPa and is used as the starting composition for the fractional crystallization simulation; (b) mineral proportion diagram for isobaric (1 GPa) fractional crystallization starting with liquid generated at 10% batch melting (Figure 8.6a). Crystallizing phases are olivine (Ol), clinopyroxene (Cpx), and spinel (Sp), in the order given. Fractionation is stopped when Mg # = 52, the observed Mg # for Lathrop Wells basalt. (abbr., amphibole (Amp), orthopyroxene (Opx), phlogopite (Phl)).

KLB-1 is shown in Figure 8.6a. The solidus at 1.5 GPa is 1120 °C; 10% batch melting is reached at ~ 1310 °C. The residual phase assemblage is olivine, orthopyroxene, spinel and clinopyroxene. All modal amphibole and phlogopite are consumed during partial melting within ≈ 30 °C of the solidus.

8.3 Fractional crystallization during ascent

The Mg # of Lathrop Wells basalt is 54 ± 2 (Perry and Straub, 1996). Given that primary liquid generated by partial melting of peridotitic sources has Mg # $\sim 75-78$, we conclude

that Lathrop Wells basalt is not primary melt. Assuming that Lathrop Wells basaltic melt originated by peridotite partial melting followed by fractional crystallization during ascent, the mean pressure of fractional crystallization can be estimated based on phase-equilibria constraints. The primary melt products of peridotite batch partial melting are used as input compositions for calculating fractional crystallization compositional paths using the MELTS and pMELTS algorithms (Ghiorso and Sack, 1995; Ghiorso *et al.*, 2002). Fractional crystallization calculations are ended when the Mg # of the computed melt is 54 ± 2 , the range observed for Lathrop Wells basalt. These calculations were performed where the source fertility, mean pressure (depth) of fractional crystallization and fraction of primary partial melt (and therefore, primary melt composition) varied systematically. Numerous fractional crystallization calculations were based on primary melt fractions of 5%, 10% and 15%, but only the fractional crystallization results based on primary melt fractions of 10% are included here, as these coincide most closely with observed Lathrop Wells major element data (Figure 8.6b). In each fractional crystallization calculation, the initial water content corresponds to that of the primary melt product of batch partial melting. The quality of the results is judged by (i) comparison of calculated melt composition oxides SiO_2 , Al_2O_3 , FeO , CaO , K_2O and Na_2O with Lathrop Wells basalt at a computed melt Mg # of 54 and (ii) comparison of the computed H_2O content of derivative melt (Mg # = 54) with the inferred water content of Lathrop Wells eruptive basalts of 2.5–4 wt. % H_2O (Detournay *et al.*, 2003). In a later section, independent methods are used based on Lathrop Wells trace element data to test the validity of the phase-equilibria constraints. In particular, a mean pressure of fractional crystallization ~ 1 GPa (depth ~ 36 km) best fits observed trace element abundances. This depth lies in the shallow upper mantle beneath YM.

8.3.1 Mean pressure and implied phase relations

Magnesium oxide variation diagrams are shown in Figure 8.7 for isobaric fractional crystallization of primary melts formed by 10% partial melting of fertile peridotite **KLB-1** (Table 8.1) at 3.5 GPa and 1.5 GPa. A sequence of fractional crystallization calculations were performed at successively higher pressures with a maximum pressure of 3.5 GPa. Predicted major element concentrations do not compare well with those measured on Lathrop Wells basalts (Perry and Straub, 1996; Valentine and Perry, 2007) for fractional crystallization at pressures above about 2 GPa. Isobaric fractional crystallization paths at both 1 GPa and 0.5 GPa are shown. The major feature is that fractional crystallization of primary partial melts formed at high pressure generates evolved melts that are too rich in FeO , CaO , and the alkalis, and too depleted in silica and alumina to match Lathrop Wells basalt. In contrast, partial melts generated at low pressure (1.5 GPa) evolve into the Lathrop Wells field during fractional crystallization at pressures in the range of 0.5 – 1.0 GPa. Liquids resulting from fractional crystallization at 1 GPa of primary melt generated at 1.5 GPa better coincide with Lathrop Wells compositions than do those resulting from lower pressure (0.5 GPa) fractional crystallization of the same primary melt. The fractionating phases at 1 GPa are olivine, clinopyroxene and spinel. At 0.5 GPa, the fractionating phases are

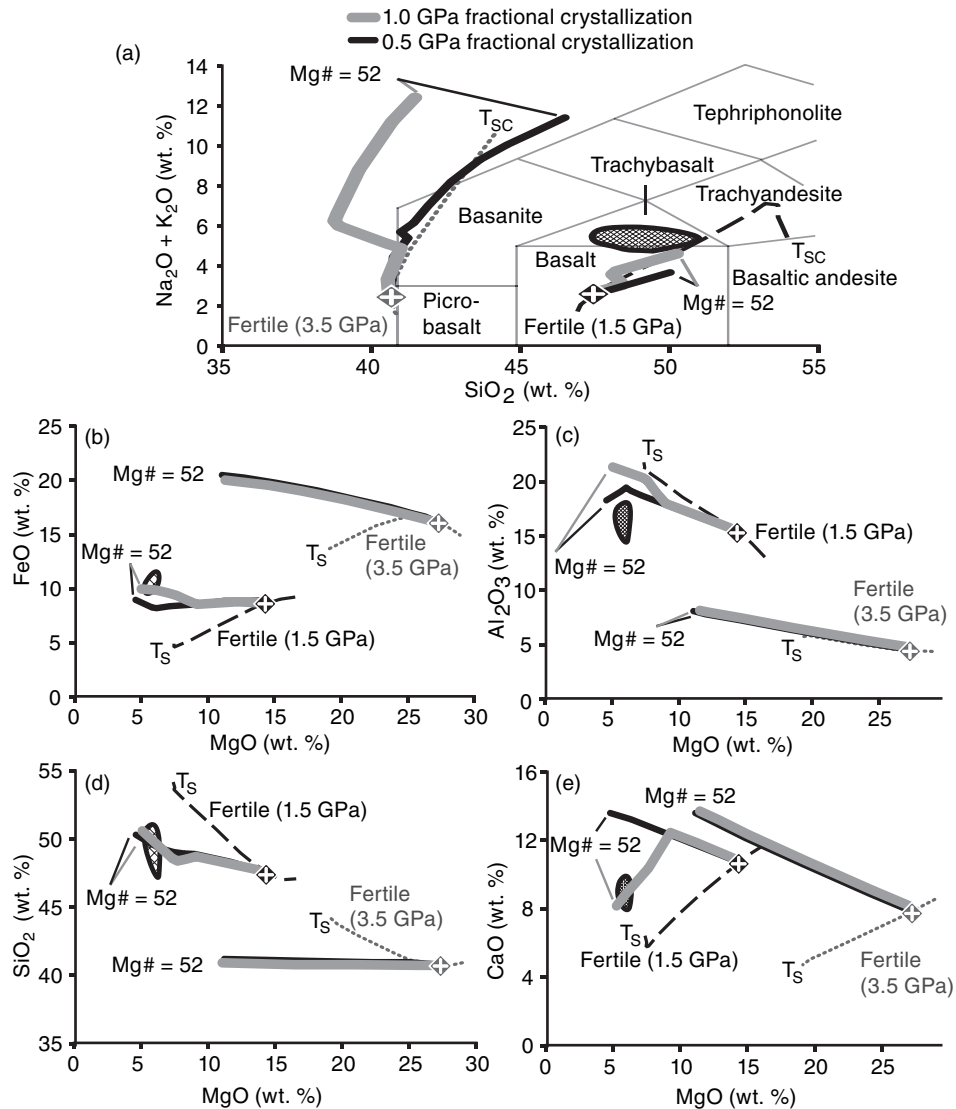


Fig. 8.7 Major element MgO variation diagrams showing Lathrop Wells data (shaded field; Perry and Straub, 1996) and pMELTS calculation results. Predicted trends represent evolution of a 10% **KLB-1** (Hirose and Kushiro, 1993) primary melt formed by batch partial melting at 1.5 (dashed black line) and 3.5 (dotted grey line) GPa by isobaric, closed-system fractional crystallization at 1.0 GPa (solid grey line) and 0.5 GPa (solid black line). Thinner lines show the results of partial melting from Figure 8.4. A cross marks the beginning of each fractional crystallization trend. Decreasing wt. % MgO and increasing wt. % ($\text{Na}_2\text{O} + \text{K}_2\text{O}$) correspond to decreasing magma temperature. The termination of each fractional crystallization trend is labeled ($\text{Mg}\# = 52$). See text for details. Note that for all oxides except alumina, the termination of the computed fractionation path lies in or very near the region of the Lathrop Wells composition for fractionation at 1 GPa of the 10% partial melt of fertile peridotite generated at 1.5 GPa.

olivine, plagioclase and trace clinopyroxene. The contrasting roles of plagioclase (low-pressure) versus clinopyroxene (high-pressure) fractionation account for the CaO–MgO variation diagram differences in Figure 8.7. In each case, the initial dissolved water content of the primary melt is 1.75 wt. % H₂O at the start of fractional crystallization. The dissolved water content of liquid at the conclusion of fractional crystallization (melt Mg # \approx 52–54) is 3.2 wt. % H₂O at 1.0 GPa and 2.6 wt. % H₂O at 0.5 GPa, within the 2.5–4.0 wt. % H₂O range of Lathrop Wells basalt pre-eruptive H₂O contents estimated by Detournay *et al.* (2003). If this exercise is repeated using 5% partial melt as the starting liquid for otherwise identical conditions, the liquid line of descent departs significantly from the Lathrop Wells field at both 1 GPa and 0.5 GPa. This is because the crystallizing phases of the 5% partial melt are dominated by olivine and amphibole. Amphibole is not found as a phenocryst in Lathrop Wells basalts.

8.3.2 Summary of solidification conditions

The composition of the Lathrop Wells basalts has been used to define an approximate set of compositional and geophysical parameters relevant to partial melting and fractional crystallization based on phase-equilibria modeling. The representative model suggests batch partial melting at \sim 50–70 km of fertile peridotite containing \approx 0.2 wt. % of H₂O, with redox conditions near the QFM-1 buffer. The extent of melting is in the range 7–10%, perhaps closer to 10% by mass. Magma ascends and undergoes fractional crystallization at a mean pressure of \approx 1 GPa (depth equivalent to 35–40 km) in the upper mantle. Because the extent of partial melting is about 10% and about half the primary melt freezes at depth, the volume of contributing source zone mantle can be estimated. The eruptive volume (dense rock equivalent of lava plus tephra) of Lathrop Wells is approximately 0.12 km³. Allowing for the effects of distal ash dispersal and the effects of solidification during ascent (\sim 50% by mass), the total volume of melt generated by partial melting in the source is liberally estimated to be \sim 0.5 km³. If the extent of partial melting was about 10 wt. %, then the mantle melting volume was \sim 5 km³. This suggests a small “melting” footprint compared to, for instance, the map distance between the southernmost and northernmost basaltic cones of the Quaternary in Crater Flats (Figure 8.1) of \sim 15 km. For example, if the melting region is assumed spherical, then the radius of the melting region is \sim 1 km.

8.4 Trace element geochemistry: a test of the phase equilibria model

It is important to test independently the conclusions of phase equilibria modeling. One test is provided by comparing trace element concentrations in Lathrop Wells basalts with predictions based on trace element modeling using the phase proportions and compositions taken from the phase equilibria model. Once the trace element abundances in the bulk source and mineral-melt partition coefficients are fixed, then the consequences of partial melting and fractional crystallization can be forward modeled by numerical solution to the equations for batch partial melting and subsequent fractional crystallization. The trace element models

Table 8.3. Initial trace element concentrations (ppm) used for trace element modeling of combined batch partial melting of **KLB-1** fertile peridotite and subsequent fractional crystallization

Element	(ppm)	Element	(ppm)	Element	(ppm)
Rb	1.90	Nd	2.67	Lu	0.043
Ba	33	Sm	0.47	Co	112
Th	0.71	Zr	21	Cr	2690
Nb	4.8	Hf	0.27	Ni	2160
Ta	0.4	Eu	0.16	Sc	12.2
La	2.60	Tb	0.07	V	56
Ce	6.29	Y	4.4	Zn	65
Sr	49	Yb	0.26		

Results presented in Figure 8.8; trace element concentrations from McDonough (1990).

are based upon the phase assemblages computed from MELTS self-consistently (Spera *et al.*, 2007). Source trace element abundances used in the calculations are collected in Table 8.3. The values of the mineral-melt trace element partition coefficients are given in Table 8.4. These data together with phase assemblages from the phase-equilibria modeling were used to compute the trace element contents of partial melts by batch melting followed by fractional crystallization. The absolute trace element abundance pattern for Lathrop Wells basalts is portrayed as a band in Figure 8.8. The starting melt composition is the point marked T₁. The cross marks the spot where the melt has a Mg # of 52. Recall that Lathrop Wells basalts have Mg # in the range 52–56. Twenty-three trace element absolute abundances have been calculated including representatives from the transition metals (e.g. Ni, Co, Cr, V), rare earth elements (La through Lu), large-ion lithophile elements (e.g. Rb, Ba, Sr, Pb) and the high-field-strength elements (e.g. Nb, Ta, Zr, Hf) among others. Overall the computed results agree well with abundances observed for Lathrop Wells basalts (Perry and Straub, 1996; Valentine and Perry, 2007). We conclude that trace element modeling based upon the major element phase equilibria results are mutually consistent.

8.5 Ascent of magma: overview

One can distinguish several dynamical regimes relevant to the segregation and upward transport of magma associated with small-volume alkali basalt lava/tephra eruptions of the Lathrop Wells type. In the source region at depths of 50–60 km, percolative flow (i.e. Darcy flow) of melt in response to small pressure gradients represents the first stage in the segregation of melt from residual crystals into networks of contiguous volumetric domains. If the melt generation rate exceeds the rate at which ductile flow can accommodate the increased volume associated with melting, magma pressure will rise above the prevailing

Table 8.4. Solid-melt partition coefficients (K_{sm}) used in partial melting and fractional crystallization trace element modeling

Element	K_{sm}					
	Phl	Cpx	Amp	OI	Opx	Sp
Rb	1.9	0.001	0.02	0.0002	0.0006	0.15
Ba	1.1	0.00011	0.1	0.0000022	0.0000036	0.028
Th	0.12	0.04	0.11	0.03	0.013	0.1
Nb	0.088	0.05	0.8	0.11	0.15	0.4
Ta	0.56	0.261	0.62	0.17	0.11	2.0
La	0.028	0.002	0.045	0.0004	0.0003	0.0029
Ce	0.03	0.017	0.09	0.0001	0.0008	0.01
Sr	0.08	0.04	0.022	0.00001	0.000511	0.077
Nd	0.0255	0.065	0.2	0.0003	0.0050	0.01
Sm	0.03	0.09	0.033	0.00014	0.0023	0.0072
Zr	2.5	0.001	0.15	0.0035	0.02	0.02
Hf	0.146	0.004	0.19	0.001	0.0063	0.14
Eu	0.03	0.09	0.3	0.001	0.0033	0.01
Tb	0.7	0.28	0.32	0.0015	0.019	0.01
Y	0.018	0.467	0.4	0.009	0.18	0.0039
Yb	0.033	0.48	0.46	0.014	0.11	1.5
Lu	0.0494	0.28	0.4	0.018	0.17	0.32
Co	23.0	1.2	13.0	2.0	3.0	8.0
Cr	5.0	5.0	30.0	1.5	10.0	11.0
Ni	1.3	1.5	1.0	6.0	1.1	29.0
Sc	8.3	2.0	2.18	0.08	1.5	0.67
V	0.5	1.81	1.49	0.06	0.6	0.5
Zn	7.0	0.49	0.69	0.86	0.41	2.6

Results shown in Figure 8.8. Data from GERM (2008), Henderson (1982), Best and Christiansen (2001). Phl (trioctahedral phyllosilicate), Cpx (clinopyroxene), Amp (amphibole), Ol (olivine), Opx (orthopyroxene), Sp (spinel).

mean normal stress, $\sigma_n(\equiv (\sigma_1 + \sigma_2 + \sigma_3)/3)$ and crack propagation will be favored. The minimum principal stress, σ_3 , is horizontal to sub-horizontal for regional transtensional stress states, and therefore vertical to sub-vertical magma-pressured cracks could open. Melt slightly above the mean normal pressure can then segregate from crystalline residue and begin ascent under the combined forces of buoyancy and small (\sim few MPa) principal stress differences. Swarms of melt-filled cracks propagating upwards transport melt at rates depending on factors such as the fracture width, fracture resistance, the driving pressure gradient and melt viscosity. It is during this stage that fractional crystallization, probably along crack margins, occurs as melt fractures rise through cooler lithospheric mantle. Rates of ascent in this stage for alkali basalts are in the range cm s^{-1} to m s^{-1} (Spera, 1986).

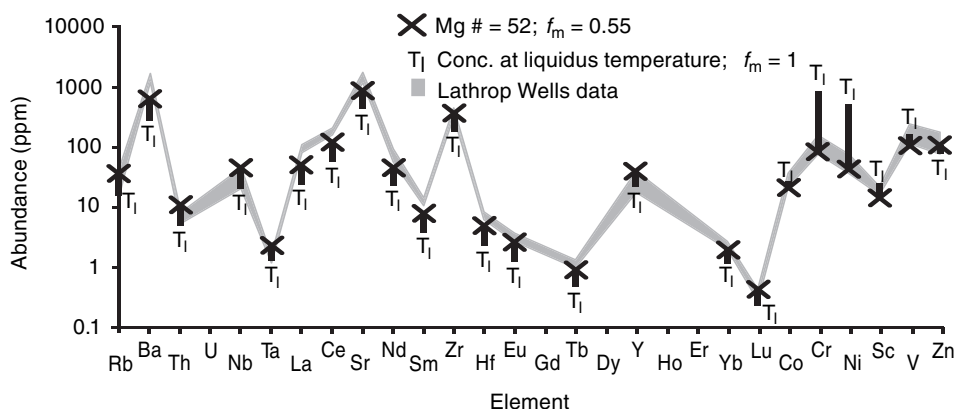


Fig. 8.8 Comparison of Lathrop Wells trace element data (absolute abundances; Perry and Straub, 1996) and calculation results based on 10% isobaric batch partial melt of **KLB-1** (Hirose and Kushiro, 1993) followed by closed-system fractional crystallization isobarically at 1 GPa terminating at a liquid Mg # = 52; symbol T_l gives the concentration of the trace element at the beginning of isobaric fractionation. The large **X** gives the trace element concentration at the end of crystal fractionation when the Mg # = 52, the low end of the small range (52–56) for Lathrop Wells. See text for details.

Alkali basalts moving at the high end of this range commonly transport ultramafic xenoliths from mantle depth to the surface. Because mantle-derived xenoliths have not been found at Lathrop Wells, mean ascent rates at mantle depths were probably in the cm s^{-1} to 0.1 m s^{-1} range. At shallow depth a transition from incompressible to compressible flow occurs due to the exsolution of volatiles triggered by magma decompression. The flow regime changes from a single phase melt flow to one with an increasing larger volume fraction of bubbles. Finally, when the volume fraction of bubbles exceeds the fragmentation limit, the flow becomes significantly compressible and accelerates upon further decompression. The incompressible to compressible flow transition is relevant to the analysis of magmatic hazards for the proposed repository.

8.5.1 Incompressible flow and thermal regime

The transport of melt in the incompressible regime has been discussed by many authors including Shaw (1980), Atkinson (1987), Pollard (1987), Spence and Turcotte (1990), Lister (1990, 1991), Lister and Kerr (1991); Rubin (1995), Takada (1994), and Heimpel and Olson (1994). Here, we draw on these to present a scale analysis specifically applicable to the eruption at Lathrop Wells. In general, two source conditions pertinent to magma transport serve as reasonable idealizations: (i) a constant volume source condition in which the magma source is rapidly depleted compared to the time required for magma transport through the crack network, and (ii) a constant discharge (volumetric rate) condition, applicable provided flow into the magma fracture plexus proceeds long after the fracture has opened. In the case

of the relatively small-volume ($\sim 10^8 \text{ m}^3$) Lathrop Wells eruption, condition (i) seems more applicable since the volume of a hypothetical single fracture of strike length 1 km and width of several meters extending to the source depth of $\sim 50 \text{ km}$ is an appreciable fraction of the entire Lathrop Wells eruptive volume. Hence buoyant fractures with constant melt volume that close at the tail are considered appropriate to magma transport feeding the Lathrop Wells eruptive fissure-vent system.

There are two limiting models for the control of the propagation speed of a magma-filled crack. If magma viscosity is the limiting factor, then although the fracture mechanics determines the crack-tip shape, the effect of the crack-tip fracture resistance on the crack propagation velocity is negligible. Models based on this concept give rise to fractures with a slightly bulging head that tapers to a narrow conduit. The crack propagation velocity is equivalent to the Poiseuille velocity of magma in the crack. In this case, the relationship between the average melt ascent velocity, \bar{v} , fracture width, h , melt viscosity, η and driving pressure gradient, $\Delta p/\ell$ is

$$\bar{v} = \frac{h^2 \Delta p}{12\eta\ell} \quad (8.1)$$

If it is assumed that melt buoyancy drives the flow ($\Delta p/\ell \sim \Delta\rho g$), then adopting the scale parameters $h = 1 \text{ m}$, $\eta = 500 \text{ Pa s}$ and $\Delta\rho = 200 \text{ kg m}^{-3}$, a typical crack propagation rate, equivalent to the magma ascent speed for this model is $\bar{v} = 0.3 \text{ m s}^{-1}$. In contrast, for buoyancy-driven crack propagation where the fracture resistance of the solid is important, the fracture velocity, v_F depends on the buoyancy of the melt and the elastic properties of the surrounding lithosphere. In particular, Heimpel and Olson (1994) found that when the melt volume in the buoyancy-driven fracture is sufficient for K_I , the mode I (tensile) crack-tip stress intensity factor (Atkinson, 1987), to exceed K_{Ic} , the mode I critical fracture toughness, unstable dynamic crack-tip propagation results. In typical dynamic fracture applications, the load is applied externally such as by external torsion, and the fracture propagation velocity rapidly approaches the elastic wave velocity of the solid, v_E , of order several km s^{-1} . However, for constant melt volume buoyancy-driven fracture propagation (the condition relevant to magma transport), the load on the crack tip is not externally defined but instead due to the body force associated with melt buoyancy within the propagating crack of height, ℓ . Therefore, for any volume of melt in the crack, the loading configuration reaches a time-averaged steady state in which the crack-tip propagation velocity is matched by the crack-tail closure velocity. The crack-tip propagation velocity in this case is

$$v_F = c \frac{v_E K_I^2}{2\ell\sigma_y^2} \left| \left(1 - \frac{K_I^2}{K_{Ic}^2} \right) \right| \quad (8.2)$$

where the mode I, stress factor K_I is

$$K_I \sim \frac{4}{\pi} \Delta p \sqrt{\frac{\pi\ell}{2}} \quad (8.3)$$

In these expressions, σ_y represents the extensional yield strength of host rock, v_E is the elastic wave propagation velocity of the lithosphere ($\sim 4 \text{ km s}^{-1}$), Δp is the difference between the magma pressure (approximately lithostatic) and the crack-normal principal stress and c is a constant of order unity in SI units. Adopting representative scale parameters for basaltic magma transport through the upper mantle lithosphere ($K_{Ic} = 300 \text{ MPa m}^{1/2}$, $v_E = 4 \text{ km s}^{-1}$, $\sigma_y = 0.3 - 1 \text{ GPa}$, $\ell = 1 \text{ km}$, $\Delta p = 1 - 10 \text{ MPa}$), the fracture propagation speed, $v_F \sim 0.1 \text{ m s}^{-1}$. One needs to remember that the stress intensity factor and fracture toughness can vary considerably in geologic media due to heterogeneity, the geometry of the crack and “process zone” effects (Lawn and Wilshaw, 1975; Kostrov and Das, 1988; Atkinson and Meredith, 1987; Rubin, 1995). It appears that magma fracture propagation speeds in the range cm s^{-1} to m s^{-1} are appropriate for alkali basalt ascent through the lithosphere. That is, the two physical models controlling ascent velocity, one limited by melt viscosity and the other by fracture propagation resistance, provide roughly comparable ascent speed estimates. The absence of ultramafic xenoliths in the Lathrop Wells eruptive products is consistent with ascent rates near the lower end of the range, perhaps $\sim 0.01 - 0.1 \text{ m s}^{-1}$. Adopting a mean ascent rate of 0.05 m s^{-1} gives a melt travel time of about two weeks from a depth of 60 km. During this period roughly half of the initial volume of magma crystallizes at depth to generate small pods or dike selvages of wehrlite (olivine + clinopyroxene cumulates). Interestingly, such ultramafic xenoliths are common at other Quaternary alkali basalt localities in the western Great Basin. The eruptive volume of Lathrop-Wells is 0.12 km^3 . Based on phase-equilibria modeling, about half of the primary melt volume crystallizes at depth. This implies transport of heat between ascending magma and the surrounding cooler lithosphere. The amount of heat transfer is estimated according to

$$Q_{\text{loss}} = \rho_m V_{\text{magma}} (C_p(T_{\text{liquidus}} - T_{\text{solidus}}) + \Delta h_{\text{cry}}) \quad (8.4)$$

where ρ_m , V_{magma} , C_p , and Δh_{cry} represent the melt density, total volume of magma generated, isobaric specific heat capacity of melt and specific enthalpy of crystallization, respectively. Adopting the parameters $\rho_m = 2800 \text{ kg m}^{-3}$, $V_{\text{magma}} = 0.12 \text{ km}^3$, $C_p = 1300 \text{ J kg}^{-1} \text{ K}$, $\Delta h_{\text{cry}} = 375 \text{ kJ kg}^{-1}$ and a liquidus to solidus temperature interval of 400 K, the total heat loss is $3 \times 10^{17} \text{ J}$ or about 125 kJ per kg of primary melt. It is reasonable to ask if this inferred heat loss based on the phase-equilibria and fracture mechanical picture is consistent with the implied requirements for heat transport. Recall that in order to match the Mg # of the Lathrop Wells basalt, roughly half of the primary melt generated by partial melting should crystallize within the lithosphere during ascent. Is this inference consistent with elementary heat transfer theory? The model involves a swarm (Shaw, 1980; Takada, 1994) of magma-filled cracks (pods) migrating upwards with concomitant heat loss to surrounding cooler lithosphere. To perform the heat transfer scale analysis, we use an estimate of the volume of a single melt-filled crack (V_c) based on fracture mechanics to determine the total number of magma-filled cracks (n_c) needed to match the Lathrop Wells eruptive volume accounting for partial solidification based on equilibria constraints. We then use results based on non-isothermal laminar flow of magma in a propagating crack

to estimate the duration of magma flow such that the required heat could be extracted. We then compare the calculated duration to the one estimated from magma ascent fracture mechanics.

The volume of a single melt-filled crack is $V_c = \ell wh$ and hence the total number (n_c) of propagating magma-filled cracks associated with the Lathrop Wells eruption is $n_c = V_T/V_c$ where ℓ is the crack height, w is the crack length (parallel to strike), h is the crack width and V_T represents the total volume of magma that freezes during ascent (roughly equal to the volume of the Lathrop Wells eruption based on phase equilibria calculations). The heat loss (\dot{Q}) for flow in a single vertically propagating crack is

$$\dot{Q} = \frac{4kNu\ell w(T_m - T_w)}{h} \quad (8.5)$$

where Nu is the nondimensional Nusselt number, equal to 7.54 (Bird *et al.*, 1987) for planar crack flow, k is the melt thermal conductivity ($0.3 \text{ W m}^{-1} \text{ K}$) and the temperature difference is the mean difference between magma and surrounding lithosphere. The total heat loss (Q_T) for an ensemble (swarm) of such propagating melt-filled cracks is

$$Q_T = \frac{V_T}{V_c} \dot{Q} t_{\text{event}} \quad (8.6)$$

where t_{event} represents the duration of the swarm migration based on the phase equilibration requirement that sufficient heat is removed from ascending magma to crystallize about half its starting mass (primary melt). Using typical parameters ($\ell = w = 1 \text{ km}$, $h = 2 \text{ m}$, $T = 500 \text{ K}$), $t_{\text{event}} \sim$ one month is estimated. This agrees with estimates based on fluid and fracture mechanics of ascent from 60 km at a mean ascent rate in the range $0.01\text{--}0.05 \text{ m s}^{-1}$ (2 months to 2 weeks). The number of melt-filled cracks that rise through the lithosphere to feed the Lathrop Wells eruption is ~ 60 in this model.

8.5.2 Compressible flow and explosive eruption regime

Magma ascent rates are approximately constant along the lithospheric ascent path because magma behaves approximately as an incompressible fluid before volatile-saturation is attained. However, because the solubility of volatile species (e.g. H_2O , CO_2 , SO_2) depends strongly on pressure, rising melt eventually becomes saturated with volatiles at some pressure, $p = p_S$, and a discrete fluid phase forms. Volatile-saturation and continued exsolution and growth of fluid bubbles initiate the regime of bubbly multiphase flow. The pressure (translated to depth with knowledge of the local stress field) at which fluid saturation occurs depends on the composition and abundance of volatiles and the dependence of volatile solubility on temperature, pressure and melt composition. At some pressure less than p_S the volume fraction of fluid in magma may exceed the critical threshold for magma fragmentation. This pressure is identified as the fragmentation pressure, $p = p_F$. In this regime, magma is fluid-dominated volumetrically and blobs of melt (pyroclasts) are carried

upwards in a rapidly expanding and accelerating fluid phase. The depth at which fragmentation takes place depends on the same parameters that control the volatile-saturation pressure and additionally on whether exsolved volatiles can leak from the magmatic mixture into the surrounding host rhyolitic tuff. The end-member scenarios are: (i) open system behavior in which volatiles are immediately and completely expelled from rising magma upon exsolution from the melt, or (ii) closed system behavior in which volatiles exsolved from the melt remain within the magmatic mixture. The dynamics of magma in the compressible regime is clearly relevant to volcanic hazard analysis and is discussed briefly below.

8.5.3 Thermodynamic volatile model

The thermodynamic mixed volatile ($\text{H}_2\text{O}-\text{CO}_2$) model of Papale (1999) is used to estimate the composition and abundance of dissolved and exsolved volatiles in melt of Lathrop Wells composition as a function of pressure, temperature and volatile bulk composition. Closed system behavior is assumed; the depth estimate for magma fragmentation is therefore a maximal value. Given the total abundance of volatiles and the bulk-system mass ratio of H_2O to CO_2 , the mass fraction of H_2O and CO_2 in coexisting volatile-saturated melt and fluid can be computed. Results exhibiting the properties of melt, fluid and magma are portrayed in Figure 8.9 for basaltic magma of Lathrop Wells composition at 1150°C with 4 wt. % total volatiles ($\text{H}_2\text{O} + \text{CO}_2$) and a bulk fluid mass ratio $\text{H}_2\text{O}/\text{CO}_2$ of 20:1. Figures 8.9a–b show the magma, fluid and melt density and viscosity as a function of pressure. Although the melt viscosity and density increase upon decreasing pressure, the viscosity (not shown) and density of the magma decrease due to the increasing volume fraction of fluid in magma upon decompression. Especially note the very rapid decrease in magma density as magma rises close to the surface. In Figure 8.9c, the variation of mass fraction and volume fraction of fluid in magma is given as a function of pressure. The critical volume fraction at fragmentation, $\theta_{\text{crit}} = 0.7$, is marked by the vertical line. This critical rheological limit is attained at a magma pressure ~ 17 MPa for the assumed parameters listed on the figure. Finally, in Figure 8.9d, the fragmentation pressure is plotted versus the total initial dissolved volatile abundance. The fragmentation pressure varies from 4 MPa to 17 MPa at 1150°C as total volatile concentrations increase from 1 wt. % to 4 wt. %.

Conversion of the saturation pressure, p_S and the fragmentation pressure, p_F to depth beneath YM requires knowledge of the state of stress with depth. Yucca Mountain lies within a region undergoing active east-southeast–west-northwest extension (Zoback, 1989). The state of stress around YM has been studied using hydraulic fracturing stress measurements, breakout and drilling-induced fractures, earthquake focal mechanisms, and fault-slip orientations (Carr, 1974; Springer *et al.*, 1984; Stock *et al.*, 1985; Rogers *et al.*, 1983; Warren and Smith, 1985; Harmsen and Rogers, 1986; Frizzell and Zoback, 1987; SNL, 1997). A review of these data is given in Stock and Healy (1988). Stress measurements at < 1.5 km depth give the ratio of horizontal to vertical stress $S_h/S_v \sim 0.35 - 0.7$. If it is assumed that S_v is lithostatic ($S_v = \rho_{\text{tuff}}gz$, ρ is the density of tuff, and z is depth), then p_S and p_F can be

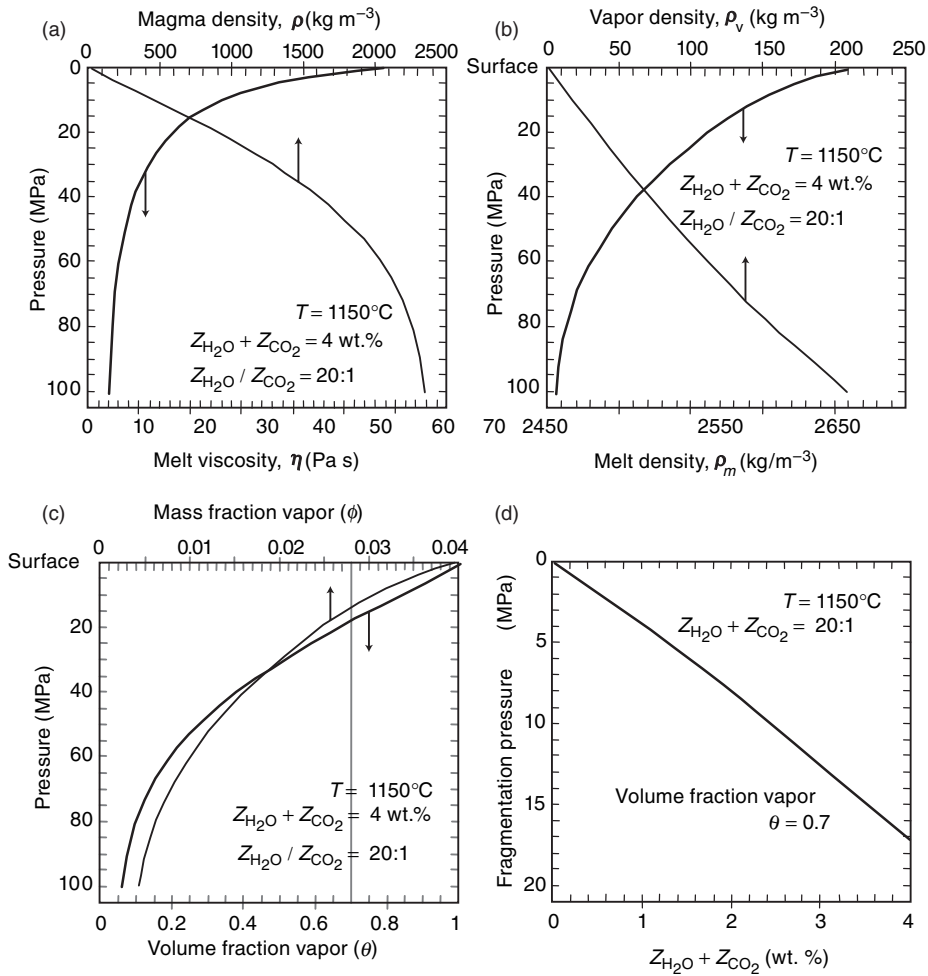


Fig. 8.9 Variation of magma properties for Lathrop Wells basaltic magma as function of pressure: (a) melt viscosity and magma density vs. pressure; (b) melt density and fluid (vapor) density vs. pressure; (c) mass fraction and volume fraction of exsolved supercritical fluid vs. pressure; (d) fragmentation pressure of Lathrop Wells basalt magma as a function of total volatile content; the fragmentation pressure is defined as the pressure at which the volume fraction of fluid equals 0.7. See text for details.

converted to depth. The dynamic constraint on magma pressure (p_m) for crack propagation is that $p_m \geq \sigma_3$. Consistent with the state of stress at YM, we assume $S_h = \sigma_3$ and $S_v = \sigma_1$ and that $S_h = \frac{2}{3}S_v$. Accordingly, the relationship between depth beneath YM and magma pressure is approximately

$$z = \frac{3p_m}{2g\rho_{\text{tuff}}}$$

Magma fragmentation pressures of 4 MPa and 17 MPa correspond to depths ~ 270 m and ~ 1300 m for total volatile contents of 1 wt. % and 4 wt. %, respectively, assuming closed-system behavior (no leakage of volatiles from magma to tuff host rock).

Finally, we can obtain an estimate of the increase in magma ascent velocity in the compressible flow regime. The theory is based on a model in which volatile-saturated magma, treated as a compressible, viscous, homogeneous pseudofluid, flows upwards in a vertical conduit of constant cross-sectional area (Spera, 1984). Magma is assumed to flow through the conduit at constant flux $\dot{M} = \rho_0 u_0$. The initial magma density and velocity are taken from the incompressible regime with $\rho_0 = 2700 \text{ kg m}^{-3}$ and $u_0 = 1 \text{ m s}^{-1}$. Scaling of the conservation of mass expression then leads to an expression for the increase in the magma velocity

$$\delta u \sim \frac{\dot{M}}{\rho^2} \delta \rho$$

between the depth of volatile saturation and the surface. With $\dot{M} = 2.7 \times 10^3 \text{ kg m}^{-2} \text{ s}$, $\delta \rho \approx 2000 \text{ kg m}^{-3}$ and $\rho \approx 250 \text{ kg m}^{-3}$ (Figure 8.9a), $\delta u \sim 90 \text{ m s}^{-1}$. Evidently, magma accelerates rapidly as the surface is approached. These magma exit velocities are consistent with eruption plumes on the order of several kilometers in height. Shallow crustal xenoliths of silicic tuff are common in the cinder cone at Lathrop Wells, consistent with the discharge rates inferred above (Doubik and Hill, 1999).

8.5.4 Compressible regime summary

In summary, the presence of a few percent by mass of dissolved volatiles in basaltic melts will ensure attainment of volatile-saturation at depths on the order of a few kilometers and magma fragmentation at depths on the order of one kilometer. If volatiles can leak out of rising magma by expulsion into surrounding country rock, the fragmentation depth will move upwards to shallower depths. The extent of upward migration of the fragmentation depth depends on the rate of fluid expulsion relative to the rate of volatile exsolution. To first order, the rate of fluid exsolution depends on the ascent rate of rising magma. This can be modeled with knowledge of the permeability of the country rock and information on the physical and thermodynamic state of rising magma; this calculation is not performed here. We have shown in Section 8.3.1 that dissolved water contents consistent with those inferred for Lathrop Wells are easily achieved provided a small amount of H_2O (e.g. 0.2 wt. %) is present in the source peridotite. The ultimate source of these fluids may be related to subduction along the western margin of the North American plate during the Mesozoic and Early Cenozoic although this is speculative. The saturation pressure (p_S) and fragmentation pressure (p_F) can be converted to depth once the state of stress in a region is specified. Beneath YM, the minimum principal stress is horizontal and the measured state of stress implies that magma fragmentation takes place at depths in the range 0.5–1.5 km depending on volatile contents assuming closed-system behavior. If volatiles do indeed escape from rising magma, then the depth at which magma fragmentation occurs will be shallower.

An eruption with a conduit anywhere within the YMR footprint would be expected to mobilize some fraction of radioactive waste; that fraction is beyond the scope of this study to estimate (see Menand *et al.*, Chapter 17, this volume; LeJuene *et al.*, Chapter 18, this volume) although we can say that the larger the eruptive volume and the higher the initial volatile-content of the magma the greater the amount of radioactive materials would be dispersed. Eruption plume heights scale with the one-fourth root of the mass discharge, $\dot{M}A_c$, where A_c is the cross-sectional area of the volcanic conduit, typically in the range 10^2 – 10^4 m² and \dot{M} is the mass flux defined in Section 8.5.3. Once in the atmosphere, ash dispersal depends very strongly on the structure of winds aloft, the particle size distribution of entrained particles and other parameters (see Volentik *et al.*, Chapter 9, this volume).

Concluding remarks

This study shows that it is possible to obtain a sketch of the thermodynamics and mechanics of magma generation, partial crystallization, ascent and eruption for small-volume alkali basaltic volcanoes. These volcanoes are typically present in continental extensional provinces such as the Great Basin of western North America where YM lies. The melting of a fertile peridotitic source containing a small amount of H₂O at depths in the range ~ 50 – 60 km followed by significant fractional crystallization (about 50% by mass) during upward ascent is consistent with the petrology, geochemistry and inferred eruptive history of Lathrop Wells volcano, a 78 ka volcanic construct of tephra and lava ~ 20 km south of the proposed nuclear waste repository. Ascent rates at depths greater than a few kilometers are in the range 0.01 – 0.1 m s⁻¹ and are limited either by the fracture toughness of the surrounding mantle or by the shear viscosity of the melt. Ascent rates are roughly constant as magma rises through the upper mantle and lower crust. At shallow depths (a few kilometers) magma contains about 3 wt. % H₂O and becomes volatile-saturated. As magma continues to ascend and decompress the volume fraction of exsolved supercritical fluid phase, dominated by H₂O component but also undoubtedly containing small amounts of CO₂ and other constituents (e.g. SO₂, H₂S, CO), rapidly increases approaching and then exceeding the fragmentation limit, provided fluid does not leak out of magma into the surrounding volcanic tuff. Around this critical rheological transition from melt-dominated to fluid-dominated magma limit, the density and viscosity of magma rapidly declines. This leads to significant magma acceleration from initial velocity of ~ 1 m s⁻¹ to final velocity (at the vent) of ~ 100 – 200 m s⁻¹. For total magma volatile contents around 3 wt. %, the fragmentation limit is reached at ~ 1 km depth, well below the depth of the proposed repository at Yucca Mountain of 300 m depth. If volatiles can escape rising magma, fragmentation depths move upwards to shallower depths.

An analytical survey of the consequences of repository disruption by magmatic processes has been presented elsewhere (Detournay *et al.*, 2003; Menand *et al.*, Chapter 17, this volume; LeJuene *et al.*, Chapter 18, this volume; Valentine and Perry, Chapter 19, this volume) although many important issues remain to be more fully explored quantitatively. Although such an analysis is beyond the scope of the present study, it is clear that quantitative

conceptual models of alkali basalt petrogenesis of the type outlined in this study form the basis of informed volcanic hazard analysis.

Further reading

Recommended reading on this subject includes articles by Shaw (1980), Spera (2000) and Ghiorso *et al.* (2002), and the section by Walker (1993) entitled Basaltic-volcano systems, in the book *Magmatic Processes and Plate Tectonics*, edited by Prichard *et al.*

Acknowledgments

We gratefully acknowledge the efforts of the Geographic Information Systems group at Los Alamos National Laboratory (LANL).

References

- Anthony, E. and J. Poths (1992). ^3He surface exposure dating and its implications for magma evolution in the Potrillo volcanic field, Rio Grande Rift, New Mexico, USA. *Geochimica et Cosmochimica Acta*, **56**(11), 4105–4108.
- Asimow, P. D. and C. H. Langmuir (2003). The importance of water to oceanic mantle melting regimes, *Nature*, **421**, 815.
- Asimow, P. D. and J. Longhi (2004). The significance of multiple saturation points in the context of polybaric near-fractional melting. *Journal of Petrology*, **45**, 2349–2367.
- Atkinson, B. K. (1987). Introduction to fracture mechanics and its geophysical applications. In: Atkinson, B. K. (ed.) *Fracture Mechanics of Rock*. London: Academic Press, 1–27.
- Atkinson, B. K. and P. G. Meredith (1987). The theory of subcritical crack growth with application to minerals and rocks. In: Atkinson, B. K. (ed.) *Fracture Mechanics of Rock*. London: Academic Press, 111–166.
- Bergman, S. C. (1982). Petrogenetic aspects of the alkali basaltic lavas and included megacrysts and nodules from the Lunar Crater Volcanic Field, Nevada, USA. Ph.D Thesis: Princeton University, USA.
- Best, M. G. and E. H. Christiansen (2001). *Igneous Petrology*. Oxford: Blackwell.
- Bird, R. B., R. C. Armstrong and O. Hassager (1987). *Dynamics of Polymeric Liquids*. New York: Wiley-Interscience.
- Bodansky, D. (1996). *Nuclear Energy: Principles, Practices and Prospects*. Woodbury, NY: American Institute of Physics.
- Carlson, R. and J. Miller (2003). Mantle wedge water contents estimated from seismic velocities in partially serpentinized peridotites. EGS–AGU–EUG Joint Assembly. Nice, France, April 6–11, 2003. #7463.
- Carr, W. J. (1974). Summary of tectonic and structural evidence for stress orientation at the Nevada Test Site, *USGS Open-File Report 74-176*. Denver, CO: US Geological Survey.
- Craig, J. R., D. J. Vaughan and B. J. Skinner (2001). *Resources of the Earth*. New Jersey: Prentice Hall.
- Crowe, B. M., G. A. Valentine, F. V. Perry and P. K. Black (2006). Volcanism: the continuing saga. In: Macfarlane, A. M. and R. C. Ewing (eds.) *Uncertainty*

- Underground: Yucca Mountain and the Nations High-Level Nuclear Waste.* Cambridge, MA: MIT Press, 131–148.
- Detournay, E., L. G. Mastin, A. Pearson, A. M. Rubin and F. J. Spera (2003). Final Report of the Igneous Consequences Peer Review Panel. Las Vegas, NV: Bechtel SAIC Company LLC Report.
- Doubik, P. and B. E. Hill (1999). Magmatic and hydromagmatic conduit development during the 1975 Tolbachik eruption, Kamchatka, with implications for hazards assessment at Yucca Mountain, NV. *Journal of Volcanological and Geothermal Research*, **91**, 43–64.
- Fleck, R. J., B. D. Turrin, D. A. Sawyer *et al.* (1996). Age and character of basaltic rocks of the Yucca Mountain region, southern Nevada. *Journal of Geophysical Research*, **101**, 8205–8227.
- Frey, F. A. and M. Prinz (1978). Ultramafic inclusions from San Carlos, Arizona: petrologic and geochemical data bearing on their petrogenesis. *Earth and Planetary Science Letters*, **38**, 129–176.
- Fridrich, C. J., J. W. Whitney, M. R. Hudson and B. M. Crowe (1999). Space–time patterns of late Cenozoic extension, vertical axis rotation, and volcanism in the Crater Flat basin, southwest Nevada. In: Wright, L. A. and B. W. Troxel (eds.) *Cenozoic Basins of Death Valley Region*, Geological Society of America Special paper 333, 197–212.
- Frizzell, V. A. and M. L. Zoback (1987). Stress orientation determined from fault slip data in the Hampel Wash area, Nevada, and its relation to contemporary regional stress field. *Tectonics*, **6**(2), 89–98.
- Geomatrix Consultants (1996). Probabilistic volcanic hazard analysis for Yucca Mountain, Nevada, Report BA0000000-1717-220-00082. San Francisco, CA: Geomatrix Consultants.
- GERM (2008). Partition Coefficient (Kd) Database. Geochemical Earth Reference Model, <http://earthref.org/GERM/index.html>.
- Ghiorso, M. S. and R. O. Sack (1995). Chemical mass transfer in magmatic processes; IV, A revised and internally consistent thermodynamic model for the interpolation and extrapolation of liquid–solid equilibria in magmatic systems at elevated temperatures and pressures. *Contributions to Mineralogy and Petrology*, **119**(2–3), 197–212.
- Ghiorso, M. S., M. M. Hirschmann, P. W. Reiners and V. C. Kress (2002). The pMELTS: a revision of MELTS for improved calculation of phase relations and major element partitioning related to partial melting of the mantle to 3 GPa. *G-Cubed—Geochemistry, Geophysics, Geosystems*, **3**(5), doi:10.1029/2001GC000217.
- Harmsen, S. C. and A. M. Rogers (1986). Inferences about the local stress field from focal mechanisms: applications to earthquakes in the southern Great Basin of Nevada. *Bulletin of the Seismological Society of America*, **76**, 1560–1572.
- Heimpel, M. and P. Olson (1994). Buoyancy-driven fracture and magma transport through the lithosphere: models and experiments. In: Ryan, M. P. (ed.) *Magmatic Systems*. New York, NY: Academic Press, 223–240.
- Henderson, P. (1982). *Inorganic Geochemistry*. Oxford: Pergamon Press.
- Hirose, K. and I. Kushiro (1993). Partial melting of dry peridotites at high pressures: determination of compositions of melts segregated from peridotite using aggregates of diamond. *Earth and Planetary Science Letters*, **114**, 477–489.
- Hirschmann, M. M., M. S. Ghiorso, L. E. Wasylenki, P. D. Asimow and E. M. Stolper (1998). Calculation of peridotite partial melting from thermodynamic models of minerals and melts. I. Review of methods and comparison to experiments. *Journal of Petrology*, **39**, 1091–1115.

- Hirschmann, M. M., P. D. Asimow, M. S. Ghiorso and E. M. Stolper (1999a). Calculation of peridotite partial melting from thermodynamic models of minerals and melts. III. Controls on isobaric melt production and the effect of water on melt production. *Journal of Petrology*, **40**, 831–851.
- Hirschmann, M. M., M. S. Ghiorso and E. M. Stolper (1999b). Calculation of peridotite partial melting from thermodynamic models of minerals and melts. II. Isobaric variations in melts near the solidus and owing to variable source composition. *Journal of Petrology*, **40**, 297–313.
- Kennedy, B. M. and M. C. van Soest (2007). Flow of mantle fluids through the ductile lower crust: helium isotope trends. *Science*, **318**, 1433–1436.
- Kostrov, B. V. and S. Das (1988). *Principles of Earthquake Source Mechanics*. Cambridge: Cambridge University Press.
- Lawn, B. R. and T. R. Wilshaw (1975). *Fracture of Brittle Solids*. Cambridge: Cambridge University Press.
- Le Maitre, R. W., P. Bateman, A. Dudek *et al.* (1989). *A Classification of Igneous Rocks and Glossary of Terms*. Oxford: Blackwell.
- Lister, J. R. (1990). Buoyancy-driven fluid fracture: the effects of material toughness and of low-viscosity precursors. *Journal of Fluid Mechanics*, **210**, 263–280.
- Lister, J. R. (1991). Steady solution for feeder dikes in a density stratified lithosphere. *Earth and Planetary Science Letters*, **107**, 233–242.
- Lister, J. R. and R. C. Kerr (1991). Fluid-mechanical models of crack propagation and their application to magma transport in dykes. *Journal of Geophysical Research*, **96**, 10 049–10 077.
- Macfarlane, A. M. and R. C. Ewing (2006). Introduction. In: Macfarlane, A. M. and R. C. Ewing (eds.) *Uncertainty Underground: Yucca Mountain and the Nations High-Level Nuclear Waste*. Cambridge, MA: MIT Press, 1–26.
- Macfarlane, A. M. and M. Miller (2007). Nuclear energy and uranium resources. *Elements*, **3**(3), 185–192.
- McDonough, W. F. (1990). Constraints on the composition of the continental lithospheric mantle. *Earth and Planetary Science Letters*, **101**, 1–18.
- Musgrove, M. and D. P. Schrag (2006). Climate history at Yucca Mountain: lessons learned from Earth History. In: Macfarlane, A. M. and R. C. Ewing (eds.) *Uncertainty Underground: Yucca Mountain and the Nations High-Level Nuclear Waste*. Cambridge, MA: MIT Press, 149–162.
- Padovani, E. R. and M. R. Reid (1989). Field guide to Kilbourne Hole maar, Dona Ana County, New Mexico. In: Chapin, C. E. and J. Zidek (eds.) *Field Excursions to Volcanic Terranes in the Western United States, Volume I. Southern Rocky Mountain Region*, Memoir 46. New Mexico Bureau of Mines and Mineral Resources, 174–185.
- Papale, P. (1999). Modeling of the solubility of a two-component H₂O + CO₂ fluid in silicate liquids. *American Mineralogist*, **84**, 477–492.
- Perry, F. V. and K. T. Straub (1996). Geochemistry of the Lathrop Wells volcanic center, Report LA-13113-MS. Los Alamos, NM: Los Alamos National Laboratory.
- Perry, F. V. and B. Youngs (2004). Characterize framework for igneous activity at Yucca Mountain, Nevada, US DOE Report ANL-MGR-GS-000001(02). Las Vegas, NV: Office of Civilian Radioactive Waste Management.
- Perry, F. V., B. M. Crowe, G. A. Valentine and L. M. Bowker (1998). Volcanism studies: final report for the Yucca Mountain project, Report LA-13478-MS. Los Alamos, NM: Los Alamos National Laboratory.

- Pollard, D. D. (1987). Elementary fracture mechanics applied to the structural interpretation of dykes. In: Halls, H. C. and W. F. Fahrig (eds.) *Mafic Dyke Swarms*, Special Paper 34. Toronto, Ontario: Geological Association of Canada, 5–24.
- Rogers, A. M., S. S. Harmsen, W. J. Carr and W. Spence (1983). Southern Great Basin seismological data report for 1981 and preliminary data analysis, USGS Open-File Report 83-699. Denver, CO: US Geological Survey.
- Rubin, A. M. (1995). Propagation of magma-filled cracks. *Annual Reviews in Earth and Planetary Science*, **23**, 287–336.
- Shaw, H. R. (1980). The fracture mechanism of magma transport from the mantle to the surface. In: Hargraves, R. B. (ed.) *Physics of Magmatic Processes*. Princeton, NJ: Princeton University Press, 201–264.
- Shaw, H. R. (1987). Uniqueness of volcanic systems. In: Decker, R. W., T. L. Wright and P. H. Stauffer (eds.) *Volcanism in Hawaii*, US Geological Survey Professional Paper 1350(2), 1357–1394.
- Smith, E. I., D. L. Feuerbach, T. R. Naumann and J. E. Faulds (1990). The area of most recent volcanism near Yucca Mountain, Nevada: implications for volcanic risk assessment. In: *High-level Radioactive Waste Management 1990*, vol. 1. New York: American Society of Civil Engineers, 81–90.
- Smith, E. I., D. L. Keenan and T. Plank (2002). Episodic volcanism and hot mantle: implications for volcanic hazard studies at the proposed nuclear waste repository at Yucca Mountain, Nevada. *GSA Today*, **12**, 4–12.
- SNL (1997). Hydraulic fracturing stress measurements in test hole ESF-AOD-HDFR#1, thermal test facility, Exploratory Studies Facility at Yucca Mountain, WA-0065. Albuquerque, NM: Sandia National Laboratories, TIC: 237818, TDIF: 305878, DTN: SNF37100195002.001.
- Spence, D. A. and D. L. Turcotte (1990). Buoyancy-driven magma fracture: a mechanism for ascent through the lithosphere and the emplacement of diamonds. *Journal of Geophysical Research*, **95**, 5133–5139.
- Spera, F. J. (1984). Carbon dioxide in petrogenesis: III. Role of volatiles in the ascent of alkaline magma with special reference to xenolith-bearing mafic lavas. *Contributions to Mineralogy and Petrology*, **88**, 217–232.
- Spera, F. J. (1986). Fluid dynamics of ascending magma and mantle metasomatic fluids. In: Menzies, M. and C. Hawkesworth (eds.) *Mantle Metasomatism*. London: Academic Press, 241–259.
- Spera, F. J. (2000). Physical properties of magma. In: H. Sigurdsson (ed.) *Encyclopedia of Volcanoes*. New York: Academic Press, 171–190.
- Spera, F. J., W. A. Bohron, C. B. Till and M. S. Ghiorso (2007). Partitioning of trace elements among coexisting crystals, melt and supercritical fluid during isobaric crystallization and melting. *American Mineralogist*, **92**(10–11), 1568–1586.
- Springer, J. E., R. K. Thorpe and H. L. McKague (1984). Borehole elongation and its relation to tectonic stress at the Nevada Test Site, Report UCRL-53528. Livermore, CA: Lawrence Livermore National Laboratory, OSTI ID 6592868.
- Stock, J. M. and J. H. Healy (1988). Stress field at Yucca Mountain, Nevada. In: Carr, M.D. and J. C. Yount (eds.) *Geologic and Hydrologic Investigation of a Potential Nuclear Waste Disposal Site at Yucca Mountain, Southern Nevada*, US Geological Survey Bulletin 1790, 87–94.
- Stock, J. M., J. H. Healy, S. H. Hickman and M. D. Zoback (1985). Hydraulic fracturing stress measurements at Yucca Mountain, Nevada, and relationship to the regional stress field. *Journal of Geophysical Research*, **90**(B10), 8691–8706.

- Takada, A. (1994). Accumulation of magma in space and time by crack interaction. In: Ryan, M. P. (ed.) *Magmatic Systems*. New York: Academic Press, 241–257.
- Thompson, G. A. and D. B. Burke (1974). Regional geophysics of the Basin and Range Province. *Annual Review of Earth and Planetary Science*, **2**, 213–238.
- Valentine, G. A. and F. V. Perry (2007). Tectonically controlled, time-predictable basaltic volcanism from a lithospheric mantle source (central Basin and Range Province, USA). *Earth and Planetary Science Letters*, **261**, 201–216.
- Valentine, G. A., G. Wolde-Gabriel, N. D. Rosenberg *et al.* (1998). Physical processes of magmatism and effects on the potential repository: synthesis of technical work through fiscal year 1995. In: Perry, F. V., B. M. Crowe, G. A. Valentine and L. M. Bowker (eds.) *Volcanism Studies: Final Report for the Yucca Mountain Project*, Los Alamos National Laboratory Report LA-13478. Los Alamos, NM: Los Alamos National Laboratory.
- Valentine G. A., F. V. Perry, D. J. Krier *et al.* (2006). Small volume basaltic volcanoes: eruptive products and processes, and post-eruptive geomorphic evolution in Crater Flat (Pleistocene), southern Nevada. *Geological Society of America, Bulletin*, **118**, 1313–1330.
- Walker, G. P. L. (1993). Basaltic-volcano systems. In: Prichard, H. M. *et al.* (eds.) *Magmatic Processes and Plate Tectonics*, Special Publication 76. London: Geological Society, 3–39.
- Warren, W. E. and C. W. Smith (1985). In situ stress estimates from hydraulic fracturing and direct observation of crack orientation. *Journal of Geophysical Research*, **90**, 6829–6839.
- Woods, A. W., S. Sparks, O. Bokhove *et al.* (2002). Modeling magma-drift interaction at the proposed high-level radioactive waste repository at Yucca Mountain, Nevada, USA. *Geophysical Research Letters*, **29**, 1–4.
- Yogodzinski, G. M., T. R. Naumann, E. I. Smith and T. K. Bradshaw (1996). Evolution of a mafic volcanic field in the central Great Basin, south central Nevada. *Journal of Geophysical Research*, **101**, 17 425–17 445.
- Zoback, M. L. (1989). State of stress and modern deformation of the northern Basin and Range Province. *Journal of Geophysical Research*, **94**(B6), 7105–7128.
- Zoback, M. L., R. E. Anderson and G. A. Thompson (1981). Cenozoic evolution of the state of stress and style of tectonism of the Basin and Range province of Western United States. *Royal Society of London Philosophical Transactions, A*, **300**, 407–434.